# Three-axis gap clearance I-PD controller design based on coefficient diagram method for 4-pole hybrid electromagnet

Kadir Erkan, Barış Can Yalçın & Muhammet Garip

Published online: 06 Oct 2017.

Submit your article to this journal ↗

Article views: 871

View related articles ↗

View Crossmark data ↗

Citing articles: 5 View citing articles ↗

OPEN ACCESS  Check for updates

# Three-axis gap clearance I-PD controller design based on coefficient diagram method for 4-pole hybrid electromagnet

Kadir Erkan, Barış Can Yalçın and Muhammet Garip

Mechatronics Engineering Department, Yıldız Technical University, Istanbul, Turkey

## ABSTRACT

4-pole hybrid electromagnetic systems have a potential usage in many industrial areas, such as clean room design, transportation, semi-conductor manufacturing due to providing mechanical contact-free operation with considerably low energy consumption. However, the main problem of magnetic levitation process: it has highly nonlinear nature and even if it can be linearized, it has unstable pole(s), which makes the system vulnerable in terms of stability. In this paper, to overcome the instability issue and track the desired references for each degree of freedom, a modified PID controller (so called I-PD) design technique based on coefficient diagram method (CDM) has been proposed. CDM is an algebraic design applied to polynomial structure of the system on the parameter space, where a specific diagram is used to present and interpret the essential data. It is quite simple to apply with a visual support, requires basic mathematical computations for field engineers, and offers a good equilibrium in terms of simplicity, stability, minimum overshoot and robustness, which are crucial specifications for maglev applications. The effectiveness and feasibility of CDM-based I-PD controller have been compared with CDM-based classical PID controller over an experimental set-up.

## 1. Introduction

U-type electromagnets have been commonly utilized in many industrial applications to suspend ferromagnetic objects. However, control applications including more than one degree of freedom cannot be possible using a standard U-type electromagnet [1]. To deal with this issue, 4-pole U-type electromagnet structure has been proposed by many researches [2–4]. This new electromagnet structure has control capacity in multi-degree of freedom with full redundancy. Each pole can generate electromagnetic force that is necessary for magnetic levitation. Energizing poles in a specific configuration allows any ferromagnetic object to move in a different axis of motion. So that, it has been used in many engineering applications requiring more than one degree-of-freedom movement, such as transportation systems, tool machines, frictionless bearings, space vehicle design, clean room design, semi-conductor manufacturing, etc. [4].

Using permanent magnets in the electromagnet structure has some crucial advantages, such as a minimized volume and a more compact structure [5,6]. Furthermore, the essential force for levitation of ferromagnetic material can be generated by only the permanent magnet(s), which means, by using hybrid electromagnets, magnetic levitation can be achieved with low energy consumption in pre-determined limits [7–9]. However, the system still needs to be stabilized [10–13]. In this study,

the zero-power control is not conducted, since the main concern is to directly control the levitation gap clearance, therefore the permanent magnets are used only as additional current-source equivalents.

Stabilization for position control can partially be achieved by using a PD-type controller. However, employment of a PD controller is a primitive approach since this type of controller adds a zero to the closed-loop transfer function which makes the system positive phase. When a system becomes positive phase, it amplifies all high-frequency inputs to the infinity. Furthermore, tracking performance of a PD-type controller is not satisfying. Because of these reasons, a more qualified controller structure is needed [14,15].

There are other types of controller structures that may be applicable to resolve the outlined issues. Even though sliding-mode-based controllers may be seen as one of the good alternatives [16], it suffers from the chattering effect. For magnetic levitation systems, robust control strategies, such as super-twisting algorithm of second-order sliding mode control or backstepping sliding mode control, can greatly weaken the system chattering [17,18]. However, these algorithms mostly reduce the linearized working space of the maglev system and require high-frequency sampling time with precise measurements.

To investigate possible advantages and disadvantages of using sliding mode control for 4-pole hybrid

---

CONTACT  Barış Can Yalçın  ✉ bcyalcin@yildiz.edu.tr

electromagnet, a simulation study about first-order integral sliding mode control of a magnetically levitated 4-pole hybrid electromagnet was conducted by our research team [19]. For reference tracking performance, it was observed that high overshoot and settling time occurred, while the system became robust against unmodelled uncertainties and external disturbances. Noise rejection is another problem for highly nonlinear maglev applications. Even though simulations may give excellent noise rejection outputs, experimental results mostly do not show the same performance.

Lack of well-organized techniques and demand for high computation capacity are the drawbacks of fuzzy logic originated approaches [20–23]. Adaptive and optimal robust control techniques require high mathematical skills and are not eligible for field engineers, since the industry is still inclined towards classical control design [10,24–27]. The main reason of this situation is that the new methods including adaptive and optimal robust control approaches are still being improved and need more time to be valid for magnetic levitation-based industrial applications.

The well-known PID controller structure can stabilize the system with relatively satisfying tracking performance, but employment of classical PID structure on the forward path transfer function introduces a closed-loop zero near the origin, which results in a large overshoot appearing at the output [28–30]. This problem can be eliminated by using the I-PD configuration of PID structure.

In [29], PID and I-PD control structures were compared for two-translational-axis motion of a 4-pole hybrid electromagnet driven by three-phase AC long stator L-PMSM. And it was proven that minimized overshoot could be well achieved with I-PD control structure.

The key of PID and I-PD design is dependent on the controller parameters, proportional, integral and derivative gains. From the practical realization point of view, the pure derivative should be avoided. Hence, the derivative term is incorporated to a low-pass filter.

There are quite a few approaches to determine the feasible PID and I-PD gains. However, classical approaches using root locus, frequency-domain methods and so on require relatively long trial-and-error steps to reach good balance of stability, tracking performance and robustness.

In this study, PID and I-PD controller gains have been chosen according to "coefficient diagram method" (CDM) for reference tracking and disturbance rejection on three different motion axes (one translational axis and two rotational axes) of 4-pole hybrid electromagnet. CDM is an algebraic design applied to polynomial structure of the system on the parameter space, where a specific visual diagram is used to present and interpret the essential data. The basic idea of this method is to use the stability index and the equivalent time constant derived from the

characteristic polynomial as the design basis [31]. The performance specification, stability index $\gamma$ and equivalent time constant $\tau$ are defined in the transfer function of the closed-loop system and related to the controller parameters algebraically in explicit form. The design methodology is quite simple and provides a good equilibrium among those of stability, tracking performance and robustness [32–34]. The advantages of CDM can be summarized as follows [35]:

- The whole controller design is quite systematic and useful. Hereby, the controller polynomials can be determined more easily than those of existing methods, such as Ziegler–Nichols method.
- Visual diagram of CDM provides an explicit interpretation of settling time, stability and parameter tuning.
- The determination of the settling time at the beginning for characteristic equations having high-order polynomials.
- Uncertainty and disturbance dynamics can be repressed with CDM without much difficulty.
- CDM can provide multi-objective design requirements.

There are two different approaches for determining CDM indices, Manabe canonical form and Kessler canonical form. Previously, by our research team, synthesizing polynomial coefficients of a zero-power controller was investigated for 4-pole hybrid electromagnet's position control and the comparison between these two approaches was conducted [36,37]. Consequently, it was proven that Manabe's approach provides lower settling time, overshoot and energy consumption.

Because of the proven success of CDM-based Manabe approach for synthesizing zero-power controller polynomial coefficients, the same approach has also been used for PID and I-PD controller polynomial coefficients in this study. The main difference between our previous study and this study is that the previous study focused only the comparison between Manabe and Kessler approaches on a zero-power control scheme, whereas this study investigates the usefulness of CDM-based Manabe approach on PID and I-PD control of a 4-pole hybrid electromagnet. Therefore, PID and I-PD control goals do not include "zero-power" aim.

The rest of the study is organized as follows: in Section 2, hybrid electromagnet dynamics are introduced. In the Section 3, PID and I-PD controller syntheses based on CDM are given, and the superiority of I-PD controller over PID controller is proven with zero-pole maps and bode magnitude plots. In Section 4, the details of the experimental set-up are conducted. In Section 5, the experimental results obtained by using both PID and I-PD controllers are given with the discussions. Finally, Section 6 concludes the paper.

## 2. Hybrid electromagnet dynamics

The electromagnet consists of four poles combined together around an iron core. Each pole consists of a coil to control the magnetic flux by means of generating an external voltage and a permanent magnet with static magnetic flux as shown in Figure 1.

In the analysis of a single coil, magnetic resistance, and the hysteresis of the iron core, eddy currents, flux leakage and fringing effects are assumed to be negligible. So that, the electromagnetic force for vertical direction is obtained as follows:

$$F_e = k \left( \frac{i + I_m}{z + L_m/\mu_r} \right)^2 \quad (1)$$

where $k$ is the configuration parameter of the electromagnet, $i$ is the coil current, $z$ is the equivalent gap, $L_m$ is the length of permanent magnets, $\mu_r$ is the relative permeability of the permanent magnet and $I_m$ is the equivalent current representation of the permanent magnet.

In Figure 2, highly nonlinear behaviour of Equation (1) is shown for the system parameters $I_m = 13.44$ A, $L_m = 3$ mm, $k = 6.84 \times 10^{-6}$ N²A² and $\mu_r = 0.004$ H.

The experimental set-up used in this study is able to achieve the levitation process in a limited working range due to the power consumption concerns occurring in large levitation gaps. So that the linearization approach is applied to Equation (1) around $z_0 = 6.8$ mm and $i_0 = 0$ A as follows:

$$K_z = -\frac{\partial F_e}{\partial z} = 2k \frac{(i + I_m)^2}{\left( z + \frac{L_m}{\mu_r} \right)^3} \quad \text{for} \ z = z_0 \ \text{and} \ i = i_0 \quad (2)$$

$$K_i = \frac{\partial F_e}{\partial i_z} = 2k \frac{(i_z + I_m)}{\left( z + \frac{L_m}{\mu_r} \right)^2} \quad \text{for} \ z = z_0 \ \text{and} \ i = i_0 \quad (3)$$

$K_z$ is the gap constant and $K_i$ is the current constant. Therefore, Equation (1) becomes

$$F_e \cong K_z \Delta z + K_i \Delta i + F_e(z_0, i_0) \quad (4)$$
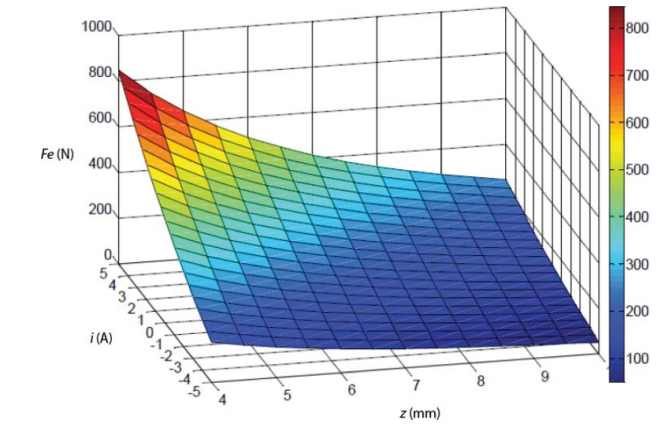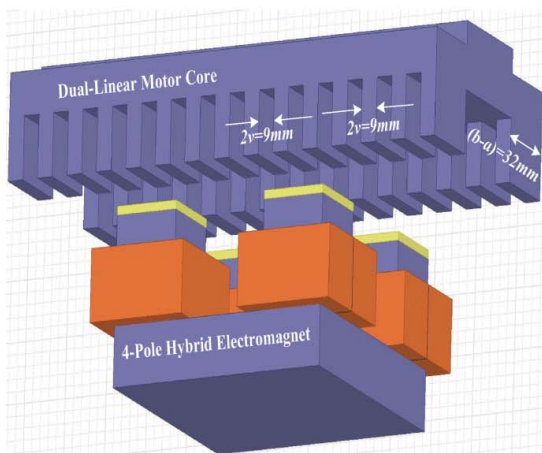


**Figure 2.** Nonlinear behavior of electromagnetic attraction force on vertical motion.

According to Newton's second law, the rate of change of momentum of the levitated mass on vertical axis can be written as follows:

$$m \frac{d^2 z}{dt^2} = F_e - mg - F_d \quad (5)$$

For the linearized equation,

$$m \frac{d^2 \Delta z}{dt^2} = K_z \Delta z + K_i \Delta i - F_d \quad (6)$$

where $m$ is the mass of the levitated object, $g$ is the gravitational acceleration and $F_d$ is the disturbance occurred due to the air viscosity.

And the system's electrical dynamics is given as follows:

$$\frac{d \Delta i}{dt} = -\frac{K_z}{K_i} \frac{d \Delta z}{dt} - \frac{R}{L} \Delta i + \frac{1}{L} \Delta V \quad (7)$$

where $V$ is the applied voltage, $L$ is the inductance and $R$ is the resistance of the drive circuit. Combining Equation (6) (without gravitational and disturbance
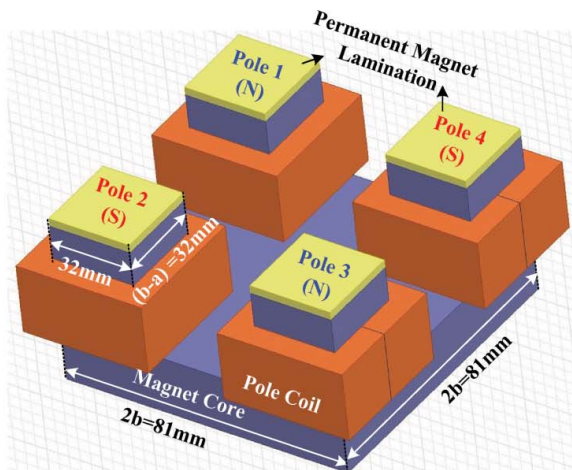


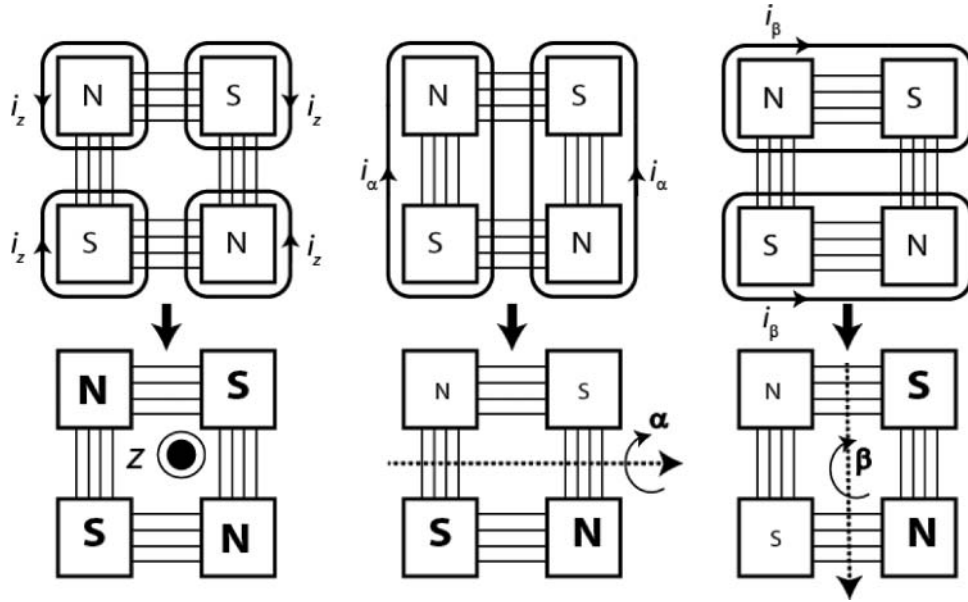**Figure 1.** (a) View-1, (b) View-2.

**Figure 3.** Energizing coils for the movement on different axes.

force) with Equation (7), the open-loop system dynamic for a single coil can be written as follows:

$$G(s) = \frac{\Delta Z(s)}{\Delta V(s)} = \frac{K_i}{mLs^3 + mRs^2 - RK_z} \quad (8)$$

The characteristic equation of the transfer function given in Equation (8) has one unstable pole. Thus, the overall system is unstable and needs to be stabilized.

The process of energizing each coil can be seen in Figure 3. Three virtual winding currents are defined as $i_z$, $i_\alpha$, $i_\beta$. These parameters represent a kind of average current working for only one axis. This assumption gives an opportunity for controlling each degree of freedom while controlling $i_1$, $i_2$, $i_3$ and $i_4$ independently.

In the second row of Figure 3, it is implied that bold and bigger characters are the energized coils; however, the system behaves as if coils are being energized with some virtual winding currents as shown in the first row of Figure 3.

Controlling 4-pole hybrid electromagnet for the translational movement $z$, $i_1$, $i_2$, $i_3$ and $i_4$ have to be positive and their average value is calculated as follows:

$$i_z = \frac{1}{4}(i_1 + i_2 + i_3 + i_4) \quad (9)$$

Controlling 4-pole hybrid electromagnet for the rotational movement $\alpha$, $i_1$ and $i_4$ have to be negative, while $i_2$ and $i_3$ have to be positive and their average value is calculated as follows:

$$i_\alpha = \frac{1}{4}(-i_1 + i_2 + i_3 - i_4) \quad (10)$$

Controlling 4-pole hybrid electromagnet for the rotational movement $\beta$, $i_1$ and $i_2$ have to be negative, while $i_3$ and $i_4$ have to be positive and their average

value is calculated as follows:

$$i_\beta = \frac{1}{4}(-i_1 - i_2 + i_3 + i_4) \quad (11)$$

Equations (9)–(11) are represented in matrix form as follows:

$$\begin{bmatrix} i_1 \\ i_2 \\ i_3 \\ i_4 \end{bmatrix} = \underbrace{\begin{bmatrix} 1 & -1 & -1 \\ 1 & 1 & -1 \\ 1 & 1 & 1 \\ 1 & -1 & 1 \end{bmatrix}}_{H} \begin{bmatrix} i_z \\ i_\alpha \\ i_\beta \end{bmatrix} \quad (12)$$

Considering the movements of all poles, vertical displacement parameter of the system along $Z$-axis is $z$, rotational displacement parameters of the system around $X$- and $Y$-axes are $\alpha$ and $\beta$, respectively. $z_1$ is the vertical displacement of pole-1, $z_2$ is the vertical displacement of pole-2, $z_3$ is the vertical displacement of pole-3, $z_4$ is the vertical displacement of pole-4. $2b$ is the magnet core width as given in Figure 1. The geometric relations are given as follows:

$$z = \frac{1}{4}(z_1 + z_2 + z_3 + z_4) \quad (13)$$

$$\alpha = \frac{1}{2b}\left(\frac{z_2 + z_3}{2} - \frac{z_1 + z_4}{2}\right) \quad (14)$$

$$\beta = \frac{1}{2b}\left(\frac{z_3 + z_4}{2} - \frac{z_1 + z_2}{2}\right) \quad (15)$$

And now, Equation (8) can be redefined for three different motion axes of the system. The transfer function for the vertical motion of the system has been given in Equation (16). $V_z$ is the sum of applied voltages for each coil, $L_z$ is the equivalent inductance and

$R_z$ is the equivalent resistance for the vertical motion along $Z$–axis:

$$G_z(s) = \frac{\Delta Z(s)}{\Delta V_z(s)} = \frac{K_i}{mL_z s^3 + mR_z s^2 - R_z K_z} \quad (16)$$

And the linearization process given in Equations (2) and (3) can be applied to rotational motions as well. $T_\alpha$ is the applied torque around $X$-axis. $K_\alpha$ is the gap constant, $K_{i\alpha}$ is the current constant for rotational movement around $X$-axis. $T_\beta$ is the applied torque around $Y$-axis. $K_\beta$ is the gap constant, $K_{i\beta}$ is the current constant for rotational movement around $Y$-axis:

$$T_\alpha = K_\alpha \Delta\alpha + K_{i\alpha}\Delta i_\alpha \quad (17)$$
$$T_\beta = K_\beta \Delta\beta + K_{i\beta}\Delta i_\beta \quad (18)$$

Therefore, the transfer function for the rotational motion of 4-pole hybrid electromagnet around $X$-axis is

$$G_\alpha(s) = \frac{\Delta\alpha(s)}{\Delta V_\alpha(s)} = \frac{K_{i\alpha}}{I_\alpha L_\alpha s^3 + I_\alpha R_\alpha s^2 - R_\alpha K_\alpha} \quad (19)$$

The transfer function for the rotational motion of 4-pole hybrid electromagnet around $Y$-axis is

$$G_\beta(s) = \frac{\Delta\beta(s)}{\Delta V_\beta(s)} = \frac{K_{i\beta}}{I_\beta L_\beta s^3 + I_\beta R_\beta s^2 - R_\beta K_\beta} \quad (20)$$

$I_\alpha$ is the moment of inertia of 4-pole hybrid electromagnet around $X$-axis and $I_\beta$ is the moment of inertia of 4-pole hybrid electromagnet around $Y$-axis. $L_\alpha$ is the equivalent inductance and $R_\alpha$ is the equivalent resistance for the rotational motion around $X$-axis. $L_\beta$ is the equivalent inductance and $R_\beta$ is the equivalent resistance for the rotational motion around $Y$-axis.

**Table 1.** The controller parameter notations.

| Controller parameter/axis | $z$ | $\alpha$ | $\beta$ |
|---|---|---|---|
| $K_P$ | $K_{P,z}$ | $K_{P,\alpha}$ | $K_{P,\beta}$ |
| $K_I$ | $K_{I,z}$ | $K_{I,\alpha}$ | $K_{I,\beta}$ |
| $K_D$ | $K_{D,z}$ | $K_{D,\alpha}$ | $K_{D,\beta}$ |
| $\tau$ | $\tau_z$ | $\tau_\alpha$ | $\tau_\beta$ |

In this study, all gap and current constants have been obtained over the test bench by several experiments and analysis.

## 3. PID and I-PD controller synthesis based on CDM

Classical PID controller adds a zero around the origin of s-plane when combined with the hybrid electromagnet transfer function given in Equation (8), which means that this situation leads to undesired excessive overshoot. To overcome this issue, PID structure has been rearranged and I-PD structure has been attained. However, in the practical sense, the realization of pure derivative term is almost impossible, owing to undesired sensor noise and effect of derivative kick. At this point, a pseudo-derivative term with a low-pass filter has been proposed. For each motion axis, an independent controller is assigned. The controller parameter notations for each motion axis have been given in Table 1. $K_P$ is the proportional gain, $K_I$ is the integral gain, $K_D$ is the derivative gain and $\tau$ is the equivalent time constant.

Because of the fact that all loop configurations are identical for three different motion axes, I-PD and PID structures for only the translational motion along $Z$-axis are given in Figure 4, and in Figure 5 to avoid unnecessary detailed information. The closed loops shown in Figures 4 and 5 are fifth-order LTI systems.

For Figure 4, the transfer function between $z_{ref}$ and $z$ is

$$\frac{Z(s)}{Z_{ref}(s)} = \frac{s(0.001K_{I,z}K_i) + K_{I,z}K_i}{s^5(0.001mL_z) + s^4(0.001mR_z + mL_z) + s^3(mR_z) + s^2(K_{D,z}K_i + 0.001K_{P,z}K_i - 0.001K_z R_z) + s(K_{P,z}K_i - K_z R_z + 0.001K_{I,z}K_i) + K_{I,z}K_i} \quad (21)$$
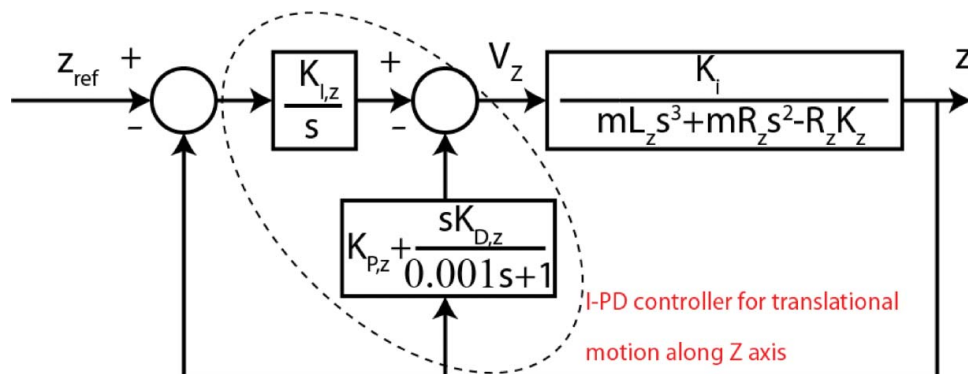


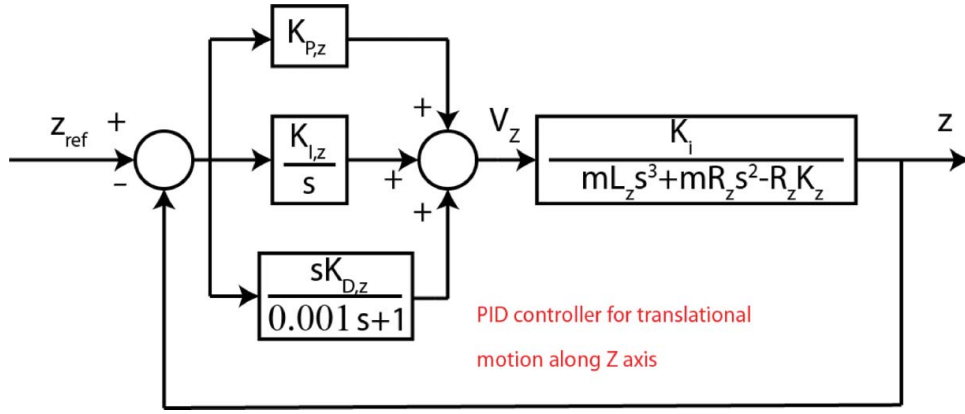**Figure 4.** I-PD controller structure for translational motion along $Z$-axis.

**Figure 5.** PID controller structure for translational motion along *Z*-axis.

When the pseudo-derivative term in Figure 4 is neglected, the transfer function between $z_{\text{ref}}$ and $z$ becomes

$$\frac{Z(s)}{Z_{\text{ref}}(s)} = \frac{K_{I,z}K_i}{s^4(mL_z) + s^3(mR_z) + s^2(K_D K_i) + s(K_{P,z}K_i - K_z R_z) + K_{I,z}K_i} \quad (22)$$

For Figure 5, the transfer function between $z_{\text{ref}}$ and $z$ is

$$\frac{Z(s)}{Z_{\text{ref}}(s)} = \frac{s^2(0.001K_{P,z}K_i + K_{D,z}K_i) + s(K_{P,z}K_i + 0.001K_{I,z}K_i) + K_{I,z}K_i}{s^5(0.001mL_z) + s^4(0.001mR_z + mL_z) + s^3(mR_z) + s^2(K_{D,z}K_i + 0.001K_{P,z}K_i - 0.001K_z R_z) + s(K_{P,z}K_i - K_z R_z + 0.001K_{I,z}K_i) + K_{I,z}K_i} \quad (23)$$

When the pseudo-derivative term in Figure 5 is neglected, the transfer function between $z_{\text{ref}}$ and $z$ becomes

$$\frac{Z(s)}{Z_{\text{ref}}(s)} = \frac{s^2(K_{D,z}K_i) + s(K_{P,z}K_i) + K_{I,z}K_i}{s^4(mL_z) + s^3(mR_z) + s^2(K_{D,z}K_i) + s(K_{P,z}K_i - K_z R_z) + K_{I,z}K_i} \quad (24)$$

The physical realization of I-PD controllers for three different axes is given in Figure 6. *T* matrix is the pseudo-inverse of *H* matrix given in Equation (12).

To obtain PID and I-PD controller gains for each motion axis, the characteristic equation of each closed-loop system has to be analysed using CDM. For simplicity, PID and I-PD controller gains are synthesized by using the characteristic equations given with Equations (22) and (24), because the pseudo-derivative term has a minor contribution on the overall system dynamics except blocking the effect of derivative kick.

The characteristic equation of a single closed-loop system can be described as

$$P(s) = a_n s^n + \cdots + a_i s^i + \cdots + a_0 \quad (25)$$

Equation (25) can be described as canonical form of Manabe for an *n*th-order polynomial as well:

$$P(s) = a_0 \cdot \left[ \left\{ \sum_{i=2}^{n} \left( \prod_{j=1}^{i-1} \frac{1}{\gamma_{j-1}^j} \right) (\tau \cdot s)^i \right\} \cdot \tau \cdot s + 1 \right] \quad (26)$$

where $a_i > 0$, for $i = 0,..., n$ are the polynomial coefficients.

$\gamma$ is defined as the stability index for $i = 1,...,.n-1$, $a_{n+1} = 0$ and $\gamma_n = \gamma_0 = \infty$:

$$\gamma_i = \frac{a_i^2}{a_{i+1}a_{i-1}} \quad (27)$$

$\gamma^*$ is defined as the stability limit:

$$\gamma_i^* = \frac{1}{\gamma_{i-1}} + \frac{1}{\gamma_{i+1}} \quad (28)$$

The equivalent time constant is

$$\tau = \frac{a_1}{a_0} \quad (29)$$

Now, the problem is here how to choose the appropriate controller parameters in terms of stability, minimum overshoot and robustness. According to Lipatov–Sokolov theorem on CDM [38], the following inequality ensures the stability, minimum overshoot and robustness for any LTI system, that is fourth or higher order:
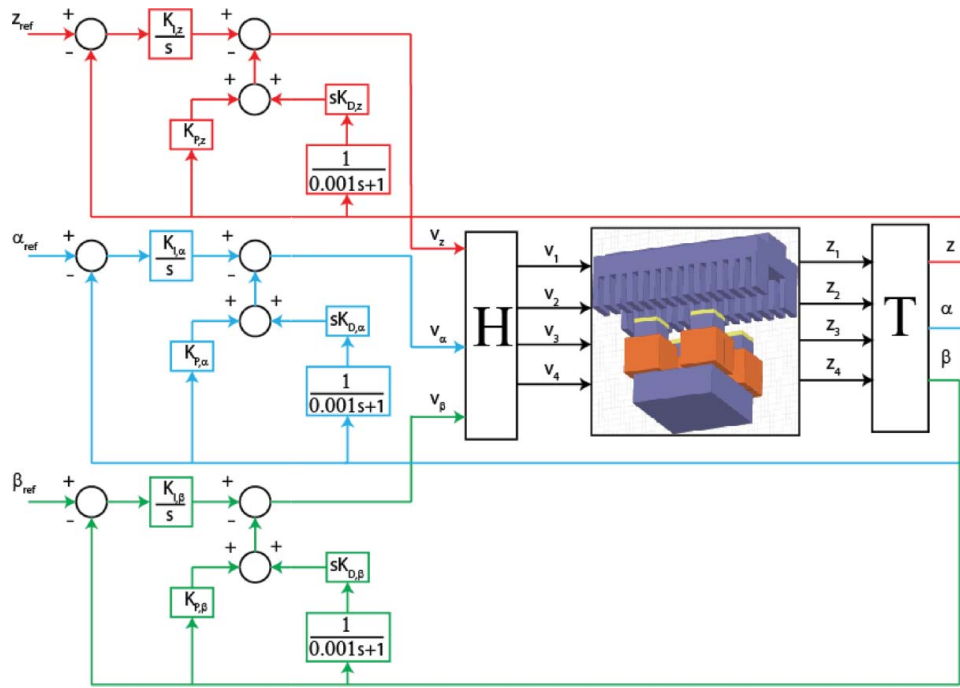
$$\gamma_i > 1.12375\gamma_i^* \quad (30)$$

**Figure 6.** Physical realization of I-PD controllers.

Manabe proposed that $\gamma_1$ should equal to 2.5, $\gamma_2$, and $\gamma_3$ should be equal to 2 to ensure the stability of fourth-order closed-loop systems [39].

To avoid unnecessary detailed information, the numerical computation of CDM controller synthesis is given for only Z-axis.

The coefficients of the characteristic equations of the closed-loop systems given with Equations (22) and (24):

$$a_4 = mL_z \tag{31}$$

$$a_3 = mR_z \tag{32}$$

$$a_2 = K_{D,z}K_i = \frac{a_3^2}{a_4\gamma_3} = \frac{(mR_z)^2}{(mL_z)\gamma_3} = \frac{mR_z^2}{L_z\gamma_3} \tag{33}$$

$$a_1 = K_{P,z}K_i - K_zR_z = \frac{a_2^2}{a_3\gamma_2} = \frac{\left(\frac{mR_z^2}{L_z\gamma_3}\right)^2}{mR_z\gamma_2} = \frac{mR_z^3}{L_z^2\gamma_3^2\gamma_2} \tag{34}$$

$$a_0 = K_{I,z}K_i = \frac{a_1^2}{a_2\gamma_1} = \frac{\left(\frac{mR_z^3}{L_z^2\gamma_3^2\gamma_2}\right)^2}{\frac{mR_z^2\gamma_1}{L_z\gamma_3}} = \frac{mR_z^4}{\gamma_3^3\gamma_2^2\gamma_1L_z^3} \tag{35}$$

By using Equations (33)–(35), the controller gains can be written as follows:

$$K_{D,z} = \frac{mR_z^2}{K_iL_z\gamma_3} \tag{36}$$

$$K_{P,z} = \frac{L_z^2\gamma_3^2\gamma_2R_zK_z + mR_z^3}{L_z^2\gamma_3^2\gamma_2K_i} \tag{37}$$

$$K_{I,z} = \frac{mR_z^4}{\gamma_3^3\gamma_2^2\gamma_1L_z^3K_i} \tag{38}$$

And the equivalent time constant is

$$\tau_z = \frac{a_1}{a_0} = \gamma_3\gamma_2\gamma_1\frac{L_z}{R_z} \tag{39}$$

As can be seen from the equations given above, the controller gains have to be chosen to meet Lipatov–Sokolov and Manabe criterions, and the equivalent time constant is dependent on the system parameters, $L_z$ and $R_z$. For the experimental set-up created in this study, the controller parameters are found as $K_{p,z} = 3050.9$, $K_{I,z} = 10714$, $K_{D,z} = 48.75$ for $\tau_z = 0.1$ for $\gamma_{1,z} = 2.5$, $\gamma_{2,z} = 2$ and $\gamma_{3,z} = 2$.

The implementation of Lipatov–Sokolov theorem and Manabe theorem into the same characteristic equations of Equations (22) and (24) gives Figure 7.

In Figure 7, the red line and the green line should not intersect each other and blue line should be convex according to CDM, otherwise stability condition becomes violated. This situation is the most advantageous property of CDM. The stability condition can be achieved not only with a mathematical approach, but
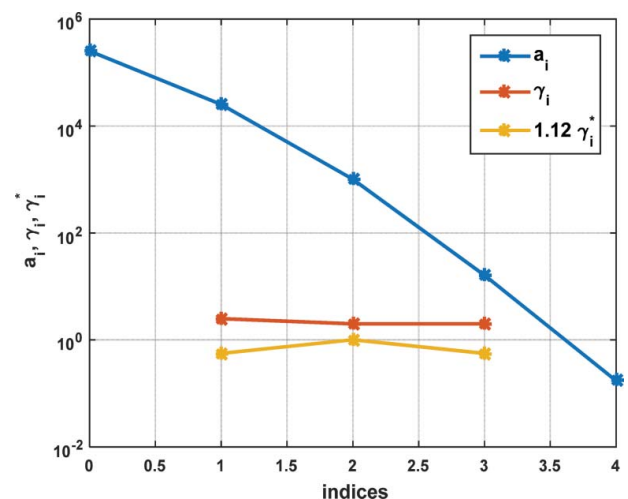


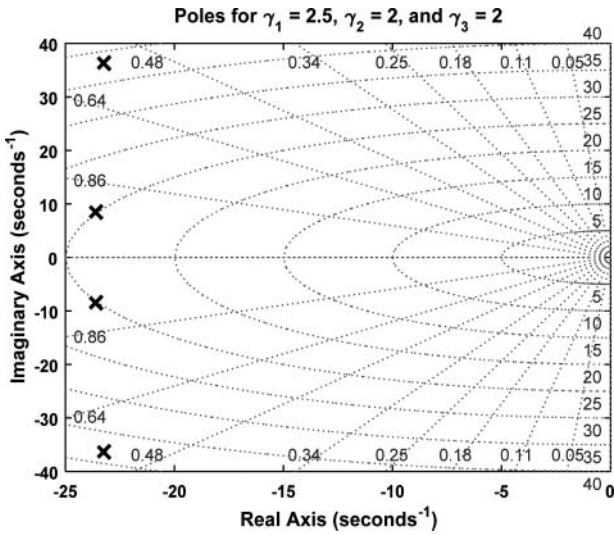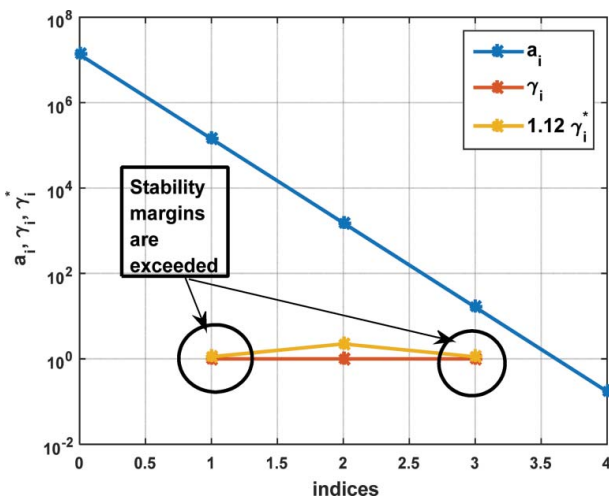**Figure 7.** CDM parameters for ensuring stability.

**Figure 8.** The roots of the closed loop for $\gamma_{1,z} = 2.5$, $\gamma_{2,z} = 2$ and $\gamma_{3,z} = 2$.

also with a visual design support. The stability condition shown with Figure 7 can also be seen in Figure 8. The roots of the closed loop are located on the left side of the imaginary axis.

An example of stability violation situation is shown in Figure 9. Instead of $\gamma_{1,z} = 2.5$, $\gamma_{2,z} = 2$ and $\gamma_{3,z} = 2$ as Manabe theorem proposed, $\gamma_{1,z} = 1$, $\gamma_{2,z} = 1$ and $\gamma_{3,z} = 1$ are used as stability index parameters. Therefore, stability index and stability limit parameters have intersection points, at the first index and at the third index, which means that the closed loop is not stable.

The instability condition shown with Figure 9 can also be seen in Figure 10. Two roots, $28.97 + 89.16j$ and $28.97 - 89.16j$, of the closed loop are located on the right side of the imaginary axis.

The stability index parameters according to Manabe theorem are given for three different motion axes in Table 2.

The physical parameters of the experimental set-up are given in Table 3.



**Figure 9.** CDM parameters for violating stability.
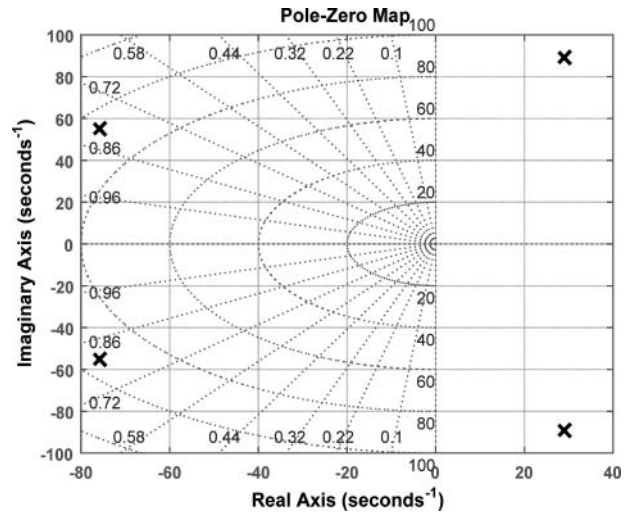


**Figure 10.** The roots of the closed loop for $\gamma_{1,z} = 1$, $\gamma_{2,z} = 1$ and $\gamma_{3,z} = 1$.

The controller gains and the equivalent time constants for $X(\alpha)$ and $Y(\beta)$ axes are calculated in the same way as calculated for $Z$-axis before. By using the values given in Table 3, CDM parameters for all three axes are calculated and given in Table 4.

For comparison between PID and I-PD controllers synthesized according to CDM-based Manabe approach, the zero-pole maps and the bode magnitude

**Table 2.** Stability index parameters.

| Stability index parameter | Value |
| --- | --- |
| $\gamma_{1,z}$ | 2.5 |
| $\gamma_{1,\alpha}$ | 2.5 |
| $\gamma_{1,\beta}$ | 2.5 |
| $\gamma_{2,z}$ | 2 |
| $\gamma_{2,\alpha}$ | 2 |
| $\gamma_{2,\beta}$ | 2 |
| $\gamma_{3,z}$ | 2 |
| $\gamma_{3,\alpha}$ | 2 |
| $\gamma_{3,\beta}$ | 2 |

**Table 3.** Experimental set-up parameters.

| Unit | Value | Unit | Value | Unit | Value |
| --- | --- | --- | --- | --- | --- |
| $m$ (kg) | 10.8 | $z_0$ (mm) | 6.88 | $\alpha_0$, $\beta_0$ (rad) | 0.0 |
| $l_{\alpha,\beta}$ (kg.m$^2$) | 0.2 | $i_0$ (A) | 0.0 | $i_{\alpha 0}$, $i_{\beta 0}$ (A) | 0.0 |
| $k$ (N$^2$/A$^2$) | $6.84 \times 10^{-6}$ | $K_z$ (N/m) | 19,811 | $K_\alpha$, $K_\beta$ (Nm/rad) | 58.10 |
| $I_m$ (A) | 13.44 | $K_i$ (N/A) | 15.57 | $K_{i\alpha}$, $K_{i\beta}$ (Nm/A) | 1.36 |
| $R_{z,\alpha,\beta}$ ($\Omega$) | 1.50 | $L_{z,\alpha,\beta}$ (H) | 0.016 | $L_m$ (mm) | 3 |

**Table 4.** CDM parameters.

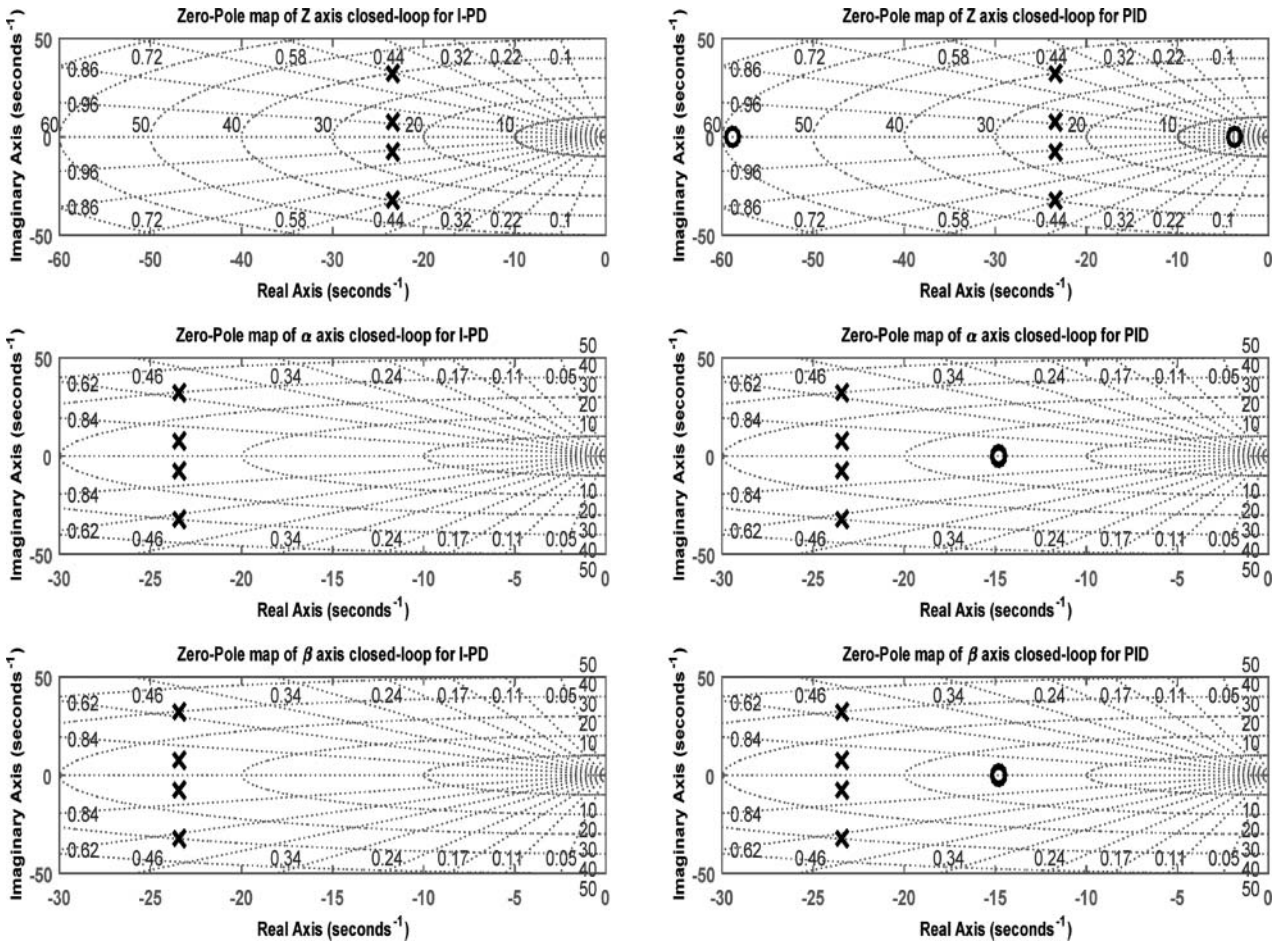| CDM gains | Value |
| --- | --- |
| $K_{P,z}$ | 3050.90 |
| $K_{I,z}$ | 10,714 |
| $K_{D,z}$ | 48.75 |
| $\tau_z$ | 0.1 |
| $K_{P,\alpha}$ | 305.26 |
| $K_{I,\alpha}$ | 2263.3 |
| $K_{D,\alpha}$ | 10.30 |
| $\tau_\alpha$ | 0.1 |
| $K_{P,\beta}$ | 305.26 |
| $K_{I,\beta}$ | 2263.3 |
| $K_{D,\beta}$ | 10.30 |
| $\tau_\beta$ | 0.1 |

**Figure 11.** Zero-pole maps.

plots of the closed loops for each axis are given in Figures 11 and 12, respectively. As can be seen from Figure 11, PID controller of each axis adds zero close to the origin, which can produce an excessive overshoot at the output of the closed loop. And for both $X(\alpha)$ axis and $Y(\beta)$ axis, two zeros coincide.

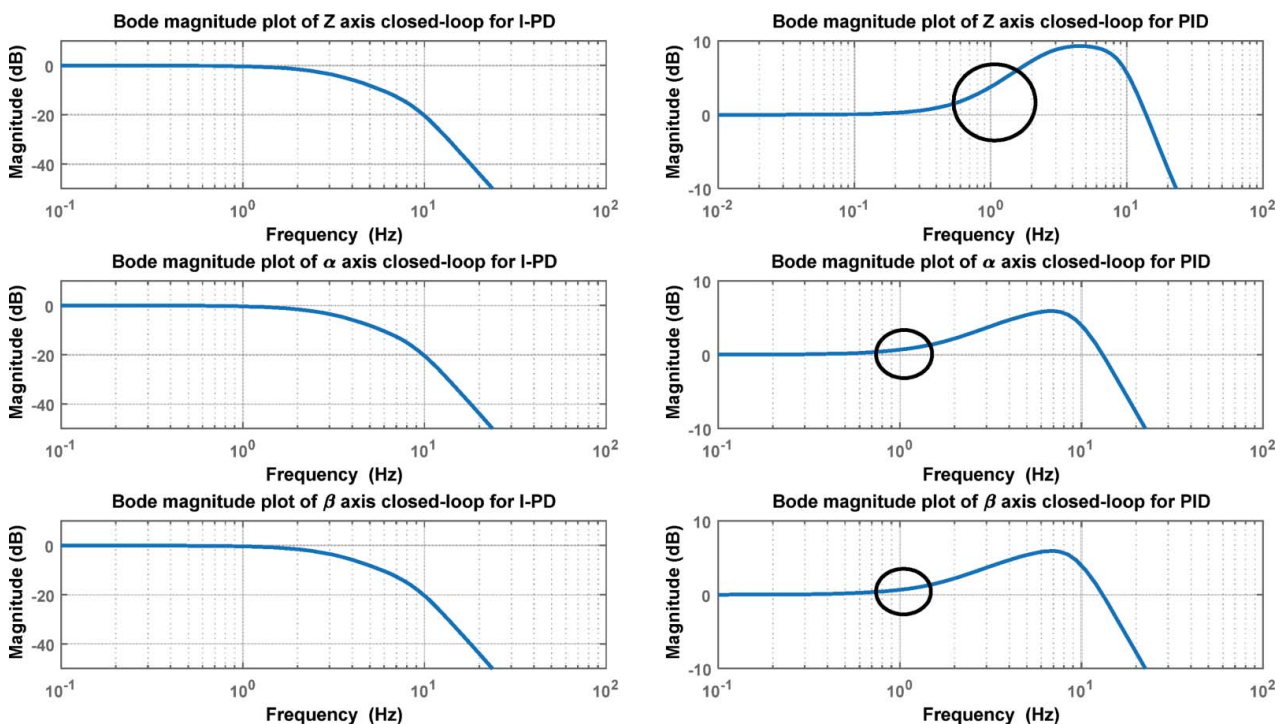For a closed-loop system, the overshoot occurring during the step reference tracking can also be observed
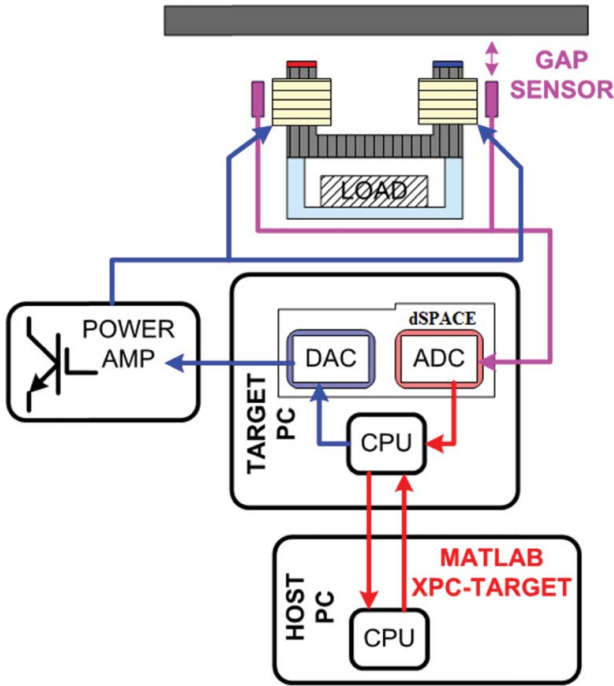


**Figure 12.** Bode magnitude plots.

**Figure 13.** The functional structure of the experimental set-up.

from the increment of the magnitude value at 1 Hz frequency on the bode magnitude plot. As can be seen from Figure 12, the magnitude values of PID configurations are higher than the magnitude values of I-PD configurations at 1 Hz. These overshoots are clearly shown in Section 5 as well.

## 4. Experimental set-up

The gap sensors produce analogue output, so that these values are being processed in dSPACE processor by means of the control algorithm designed in MATLAB/Simulink environment. XPC-TARGET has been used for rapid prototyping purpose. The functional structure of the experimental set-up can be seen in Figure 13.

The overall experimental set-up can be seen in Figure 14. It consists of 4-pole hybrid electromagnet, Host PC, Target PC, dSPACE and power amplifiers.

The structure of 4-pole hybrid electromagnet and gap sensors can be seen in Figure 15.
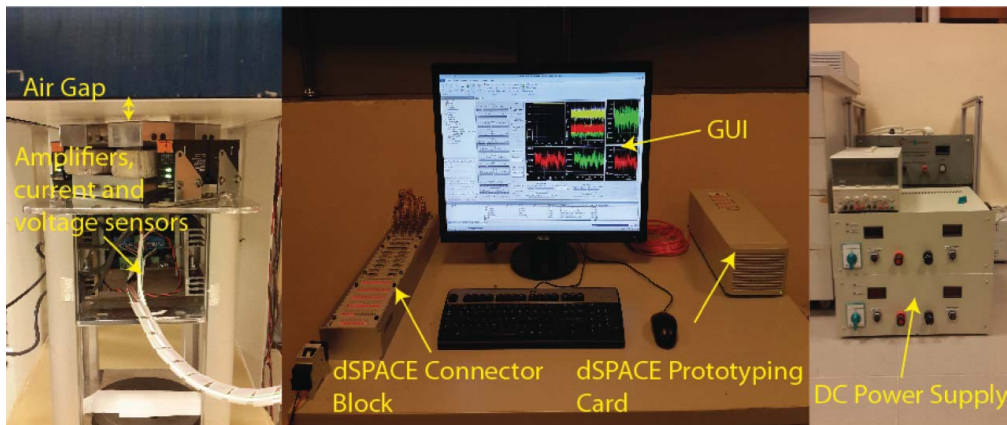


**Figure 14.** The overall experimental set-up.
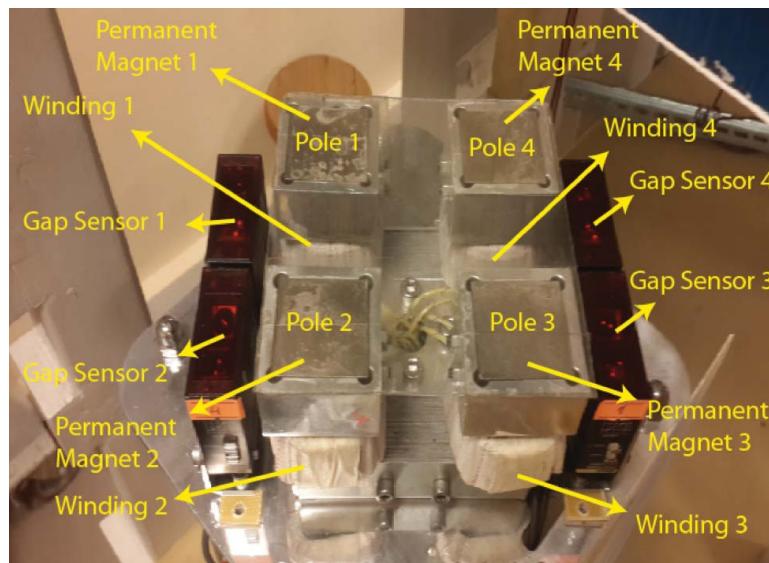


**Figure 15.** The structure of 4-pole hybrid electromagnet poles and gap sensors.
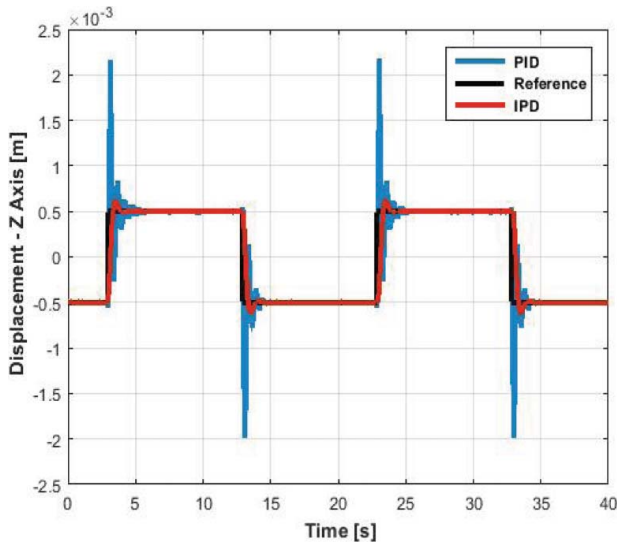
**Figure 16.** Reference tracking performances of CDM-based PID and I-PD controllers along Z-axis.

## 5. Experiments and results

### 5.1. Step reference tracking

The reference tracking performance of PID and I-PD controllers is tested using step input references by four different experiments. In the first experiment, $z_{ref}$ is a step input with 1 mm magnitude and 20 s period, $\alpha_{ref}$ and $\beta_{ref}$ are zero. In the second experiment, $\alpha_{ref}$ is a step input with 0.01 rad magnitude and 20 s period, $z_{ref}$ and $\beta_{ref}$ are zero. In the third experiment, $\beta_{ref}$ is a step input with 0.01 rad magnitude and 20 s period, $z_{ref}$ and $\alpha_{ref}$ are zero. In the fourth experiment, 3-dof reference tracking is conducted. Each reference, $\alpha_{ref}$, $\beta_{ref}$ and $z_{ref}$, are chosen step inputs varying at different periods for evaluating both PID and I-PD performances under harsh conditions, $z_{ref}$ is a step input with 1 mm magnitude and 20 s period, $\alpha_{ref}$ is a step input with 0.01 rad
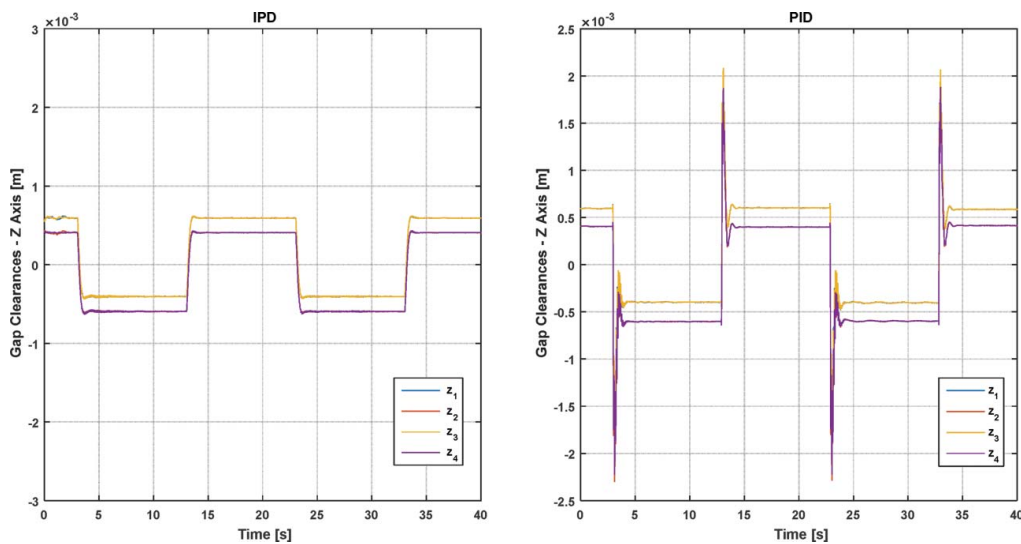


**Figure 17.** $z_1$, $z_2$, $z_3$ and $z_4$ parameters occurring during Z-axis reference tracking for I-PD and PID controllers.
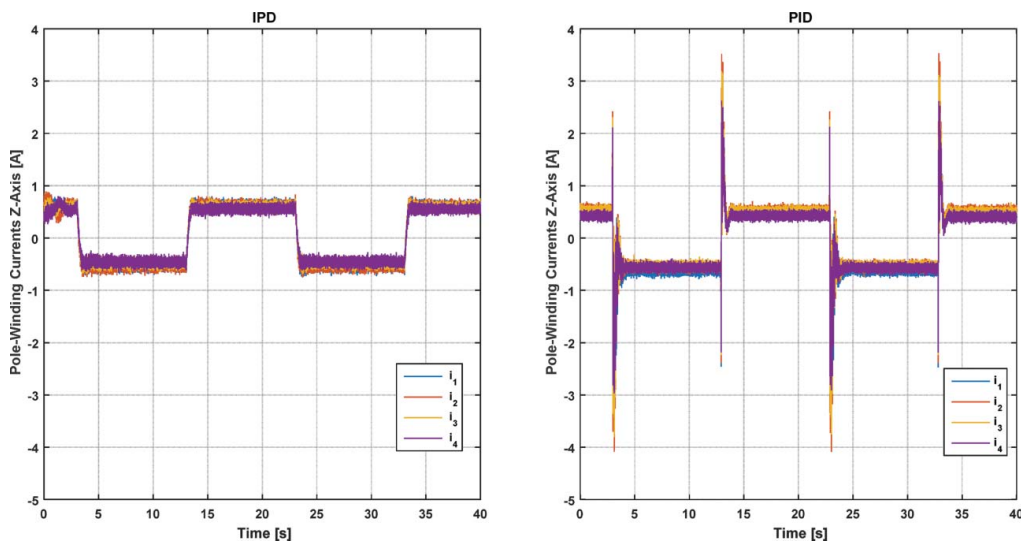


**Figure 18.** $i_1$, $i_2$, $i_3$ and $i_4$ parameters occurring during Z-axis reference tracking for I-PD and PID controllers.
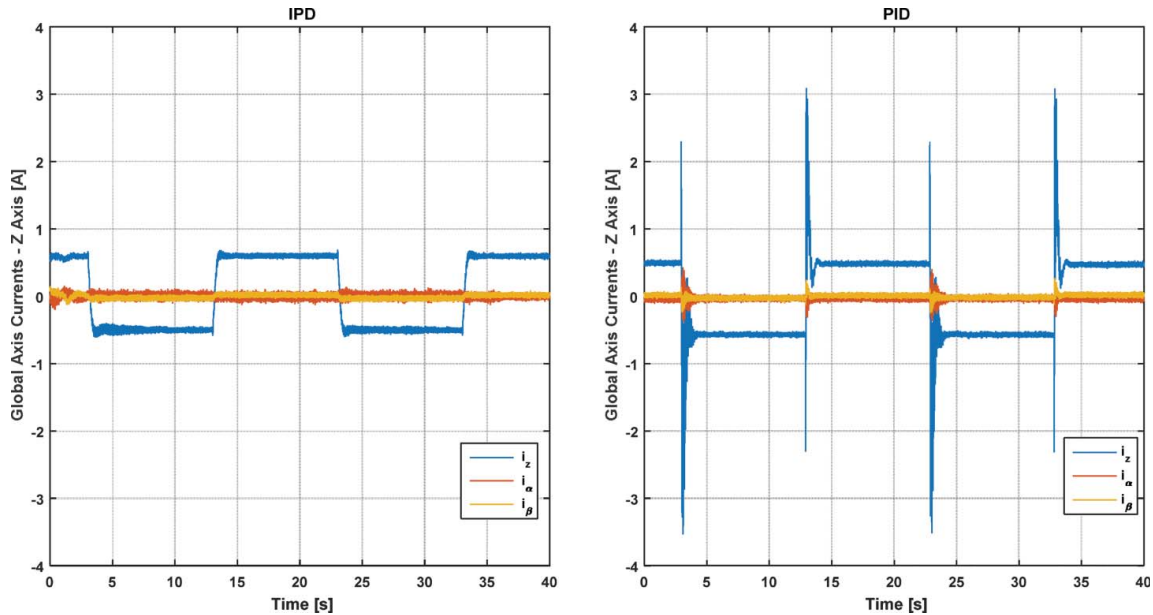
**Figure 19.** $i_z$, $i_\alpha$ and $i_\beta$ parameters occurring during Z-axis reference tracking for I-PD and PID controllers.
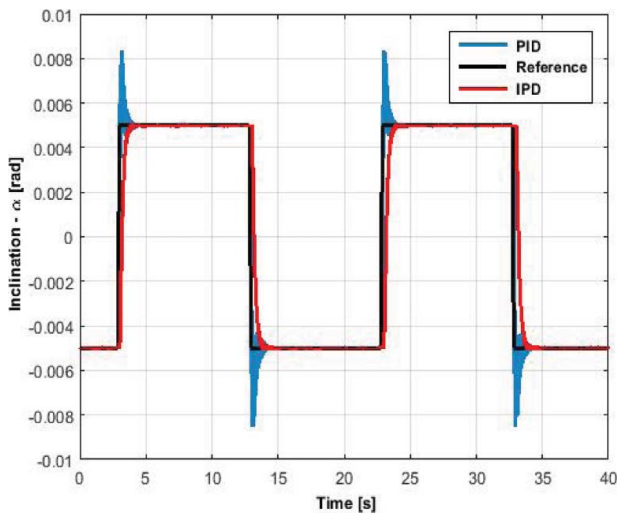


**Figure 20.** Reference tracking performances of CDM-based PID and I-PD controllers around $X(\alpha)$ axis.

magnitude and 15 s period, $\beta_{ref}$ is a step input with 0.01 rad magnitude and 10 s period.

The outputs of the first experiment are given in Figures 16–19. As can be seen in Figure 16, PID controller gives undesired excessive overshoots, whereas I-PD controller performs almost a perfect tracking performance for Z-axis.

In Figure 17, $z_1$, $z_2$, $z_3$ and $z_4$ parameters occurring during Z-axis reference tracking are shown. These values are being measured by gap sensors and sent into $T$ matrix, shown in Figure 6, and $T$ matrix produces $z$, $\alpha$, $\beta$ values for feedback into the controller. Because of $z$ is arithmetic mean of $z_1$, $z_2$, $z_3$ and $z_4$, PID overshoots shown in Figure 16 are arithmetic means of PID overshoots shown in Figure 17. The differences between $z_1$, $z_2$, $z_3$ and $z_4$ parameters are caused by several reasons, such as sensor noise, faults in mechanical structure,
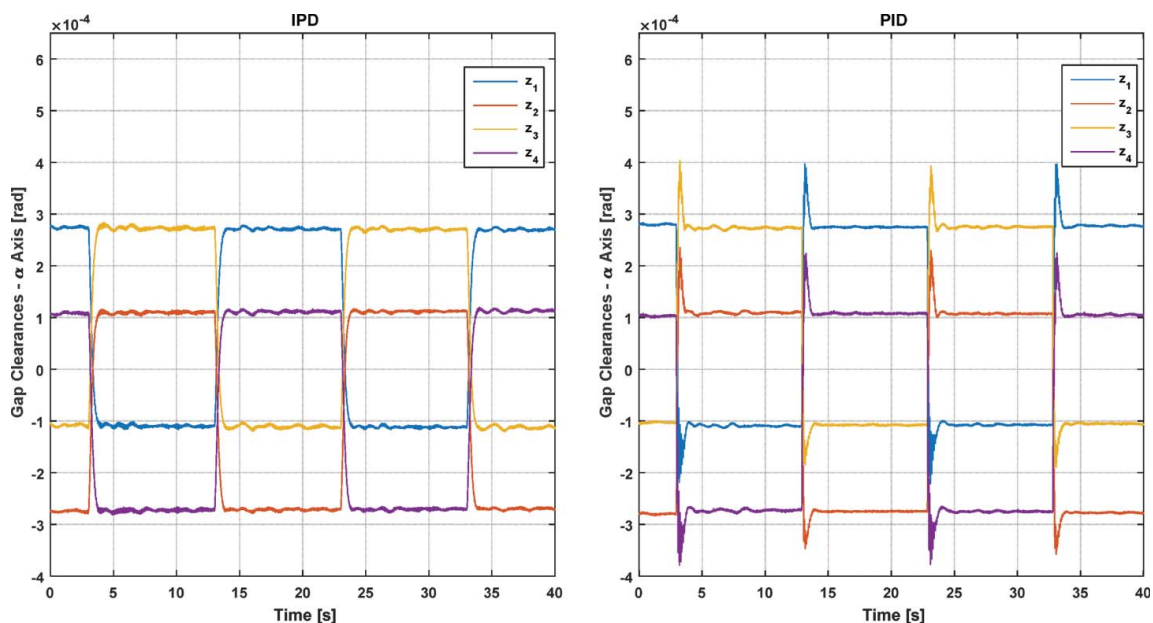


**Figure 21.** $z_1$, $z_2$, $z_3$ and $z_4$ parameters occurring during $X(\alpha)$ axis reference tracking for I-PD and PID controllers.
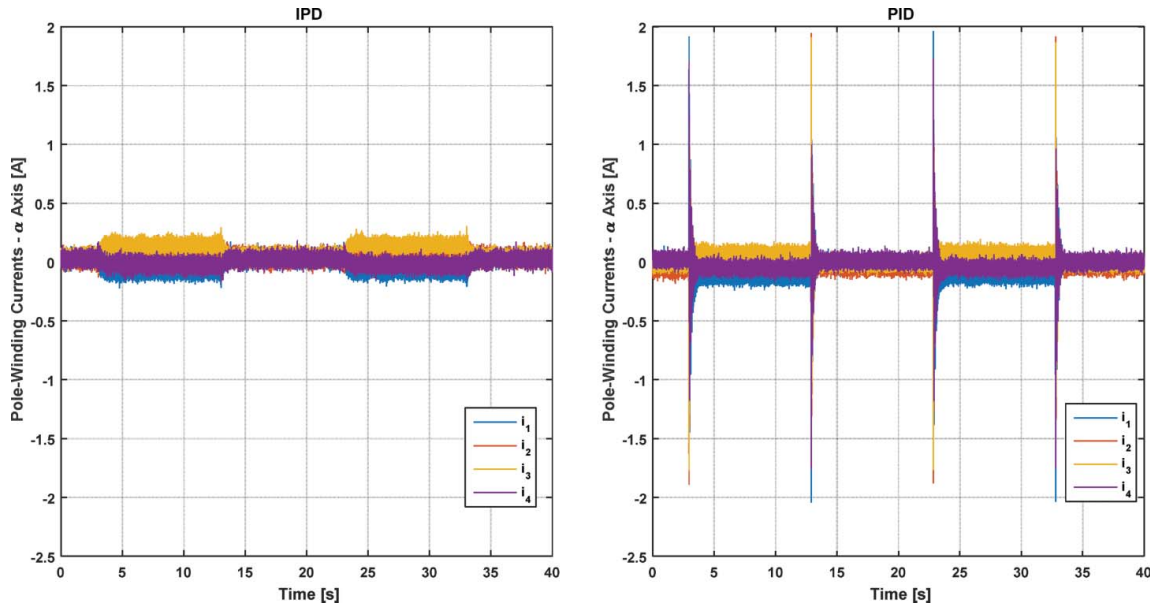
**Figure 22.** $i_1$, $i_2$, $i_3$ and $i_4$ parameters occurring during $X(\alpha)$ axis reference tracking for I-PD and PID controllers.
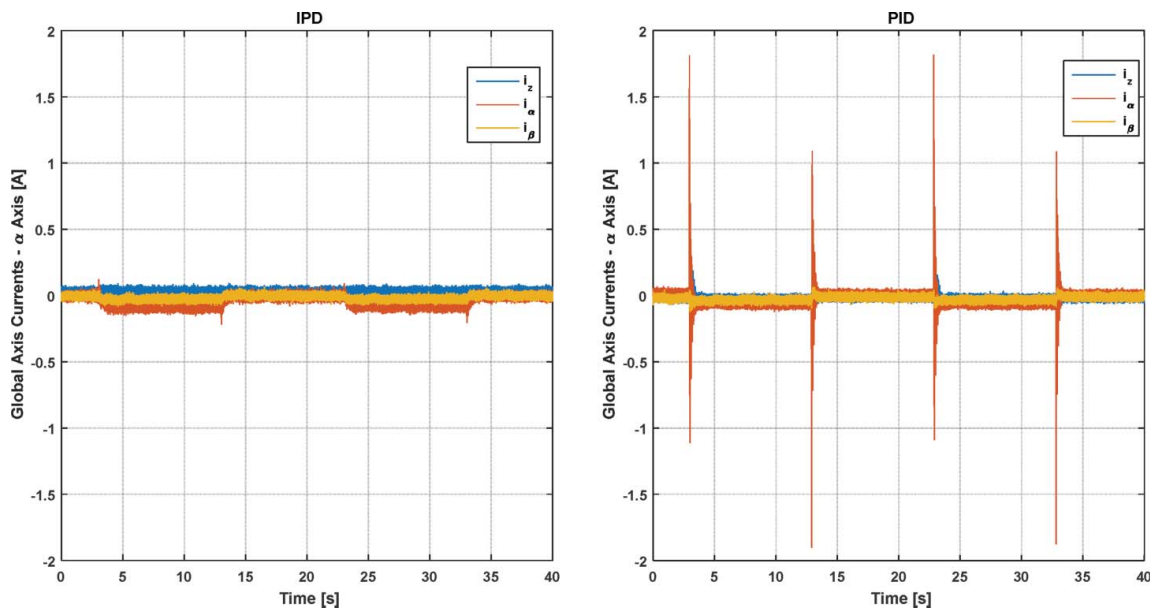


**Figure 23.** $i_z$, $i_\alpha$ and $i_\beta$ parameters occurring during $X(\alpha)$ axis reference tracking for I-PD and PID controllers.

etc. However, their dimensions are very small. Therefore, the differences do not affect the overall performance.

In Figure 18, $i_1$, $i_2$, $i_3$ and $i_4$ parameters occurring during $Z$-axis reference tracking are shown. These values are measured by the current sensors. During the overshoots by PID controller given in Figure 16, the system needs more energy; therefore, the overshoots of the current values start occurring as well. The overshoots of the current values may harm the current sensor board. Hereby, I-PD controller is more applicable.

In Figure 19, the global-axis currents for $Z$-axis reference tracking are shown. These values are calculated in $T$ matrix using $i_1$, $i_2$, $i_3$ and $i_4$ parameters. Because of $i_z$ is arithmetic mean of $i_1$, $i_2$, $i_3$ and $i_4$, as given in Equation (9), the overshoots shown in Figure 19 are arithmetic means of the overshoots shown in Figure 18.
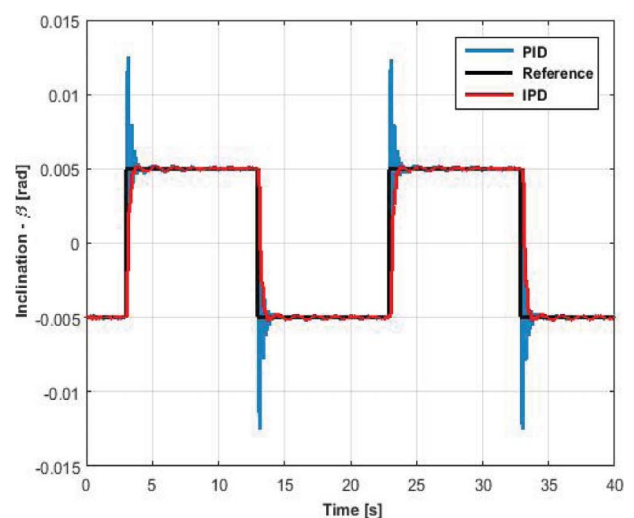


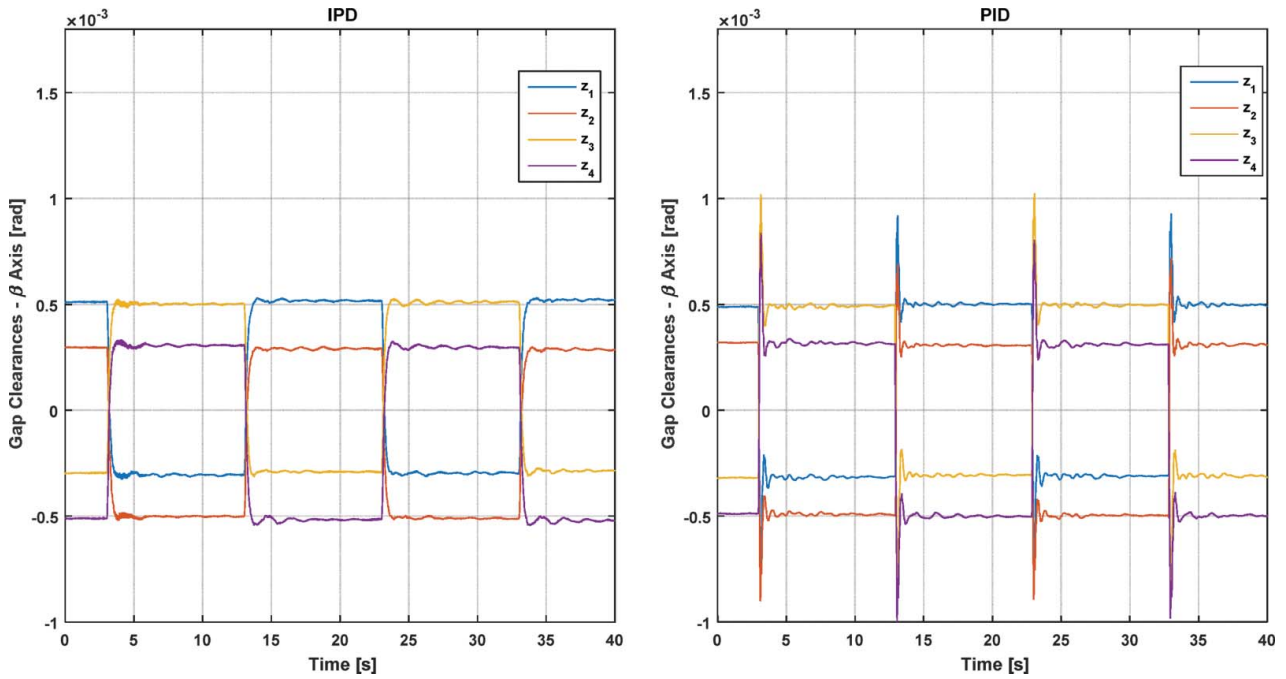**Figure 24.** Reference tracking performances of CDM-based PID and I-PD controllers around $Y(\beta)$ axis.

**Figure 25.** $z_1$, $z_2$, $z_3$ and $z_4$ parameters occurring during $Y(\beta)$ axis reference tracking for I-PD and PID controllers.

And because of the movement is only along $Z$-axis, $i_\alpha$ and $i_\beta$ are measured around zero.

The outputs of the second experiment are given in Figures 20–23. As can be seen in Figure 20, PID controller gives undesired excessive overshoots, whereas I-PD controller performs almost a perfect tracking performance for $X(\alpha)$ axis.

In Figure 21, $z_2$ and $z_3$ increase, while $z_1$ and $z_4$ decrease for each positive edge of the step input, and $z_2$ and $z_3$ decrease while $z_1$ and $z_4$ increase for each negative edge of the step input. This geometric relation was also given in Equation (14).

In Figure 22, $i_1$, $i_2$, $i_3$ and $i_4$ parameters occurring during $X(\alpha)$ axis reference tracking are shown. $i_2$ and $i_3$ increase while $i_1$ and $i_4$ decrease for each positive edge of the step input, $i_2$ and $i_3$ decrease while $i_1$ and $i_4$ increase for each negative edge of the step input.

In Figure 23, the global-axis currents for $X(\alpha)$ axis reference tracking are shown. Because of the movement is only around $X(\alpha)$ axis, $i_z$ and $i_\beta$ are measured around zero.

The outputs of the third experiment are given in Figures 24–27. As can be seen in Figure 24, PID controller gives undesired excessive overshoots, whereas
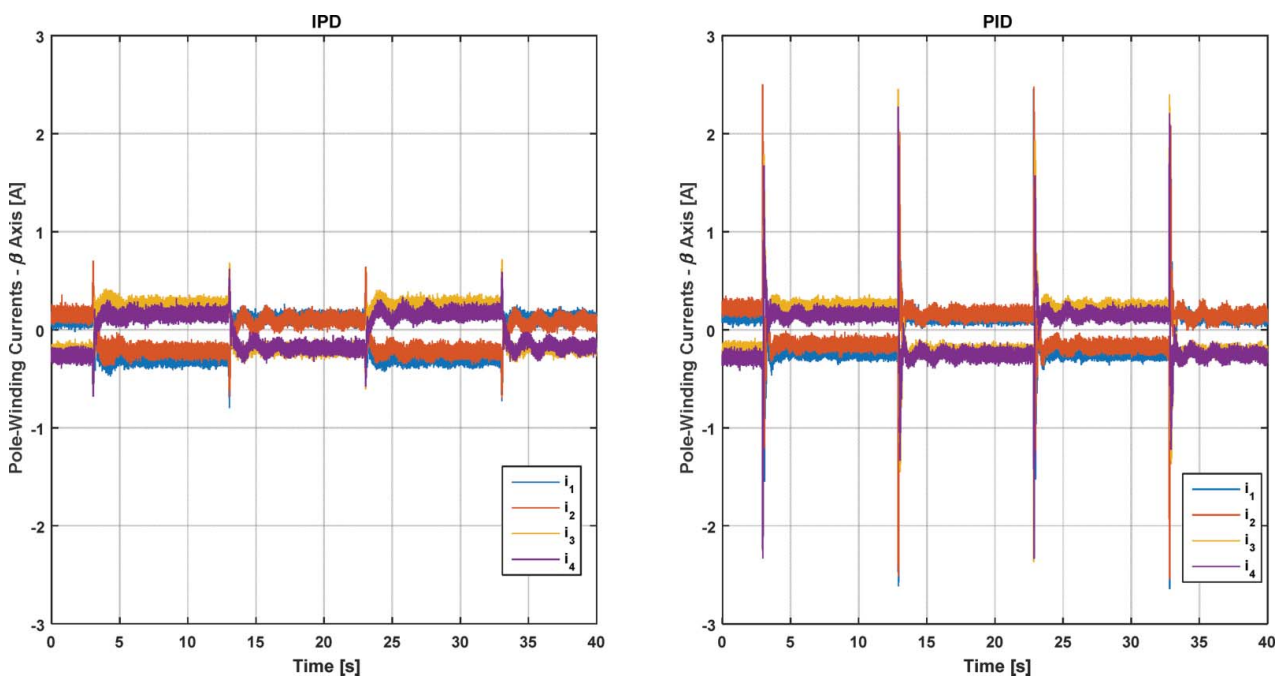


**Figure 26.** $i_1$, $i_2$, $i_3$ and $i_4$ parameters occurring during $Y(\beta)$ axis reference tracking for I-PD and PID controllers.
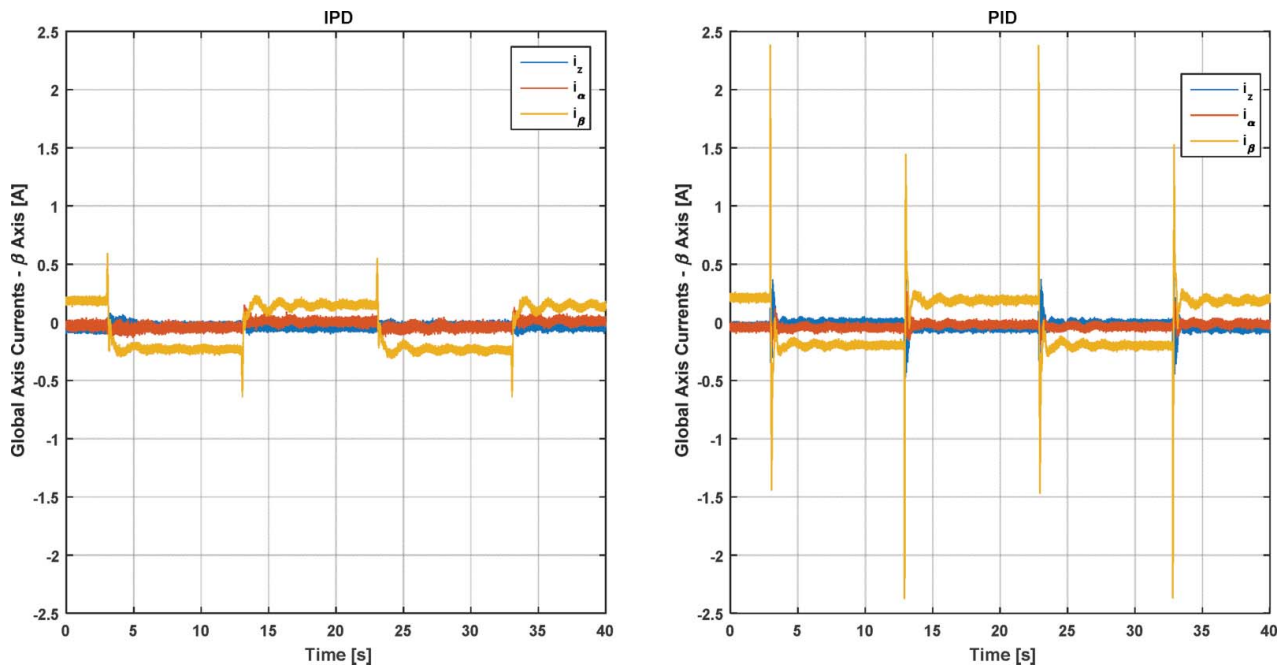
**Figure 27.** $i_z$, $i_\alpha$ and $i_\beta$ parameters occurring during $Y(\beta)$ axis reference tracking for I-PD and PID controllers.

I-PD controller performs almost a perfect tracking performance for $Y(\beta)$ axis.

In Figure 25, $z_3$ and $z_4$ increase while $z_1$ and $z_2$ decrease for each positive edge of the step input, and $z_3$ and $z_4$ decrease while $z_1$ and $z_2$ increase for each negative edge of the step input. This geometric relation was also given in Equation (15).

In Figure 26, $i_1$, $i_2$, $i_3$ and $i_4$ parameters occurring during $Y(\beta)$ axis reference tracking are shown. $i_3$ and $i_4$ increase while $i_1$ and $i_2$ decrease for each positive edge of the step input, and $i_3$ and $i_4$ decrease while $i_1$ and $i_2$ increase for each negative edge of the step input.

In Figure 27, the global-axis currents for $Y(\beta)$ axis reference tracking are shown. Because of the movement is only around $Y(\beta)$ axis, $i_z$ and $i_\alpha$ are measured around zero.
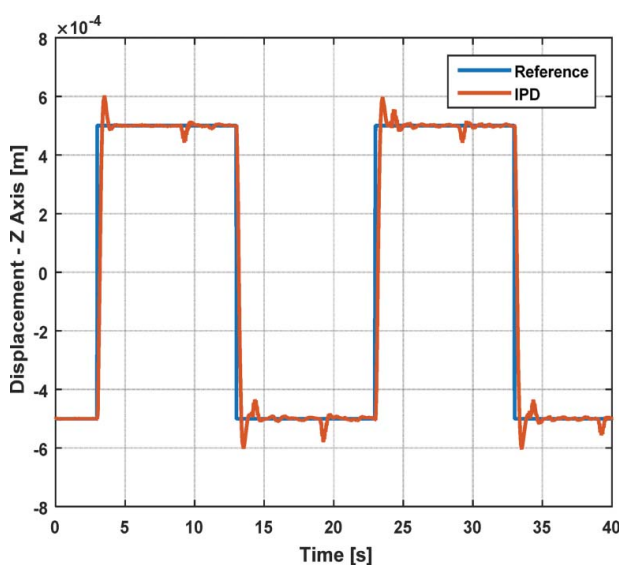
The current values measured in Figures 22 and 23 are considerably close to each other, whereas the current values measured in Figures 26 and 27 are not. The main reason of this situation is the noise effect of the current sensors occurring differently for each motion axis.

After proving the superiority of I-PD controller over PID controller for step reference tracking, the fourth experiment is conducted for only I-PD controller. The outputs of the fourth experiment are given in Figures 28–33. As can be seen from Figures 28–30, CDM-based I-PD controllers perform almost a perfect tracking performance for each degree of freedom during 3-dof motion. The oscillations after settling are caused by the delay time between each step reference. There is
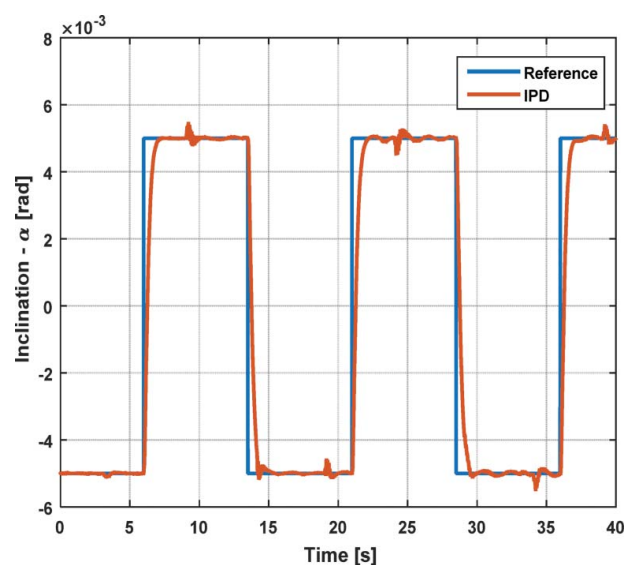


**Figure 28.** Reference tracking performance of CDM-based I-PD controller along Z-axis for 3-dof motion.



**Figure 29.** Reference tracking performance of CDM-based I-PD controller around $X(\alpha)$ axis for 3-dof motion.
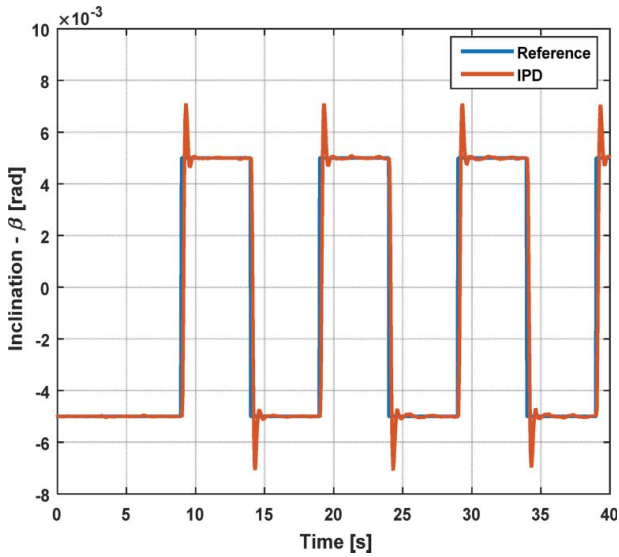
**Figure 30.** Reference tracking performance of CDM-based I-PD controller around $Y(\beta)$ axis for 3-dof motion.

3 s delay time between $z_{ref}$ and $\alpha_{ref}$, and 6 s delay time between $z_{ref}$ and $\beta_{ref}$.

In Figure 31, $z_1$, $z_2$, $z_3$ and $z_4$ parameters occurring during 3-dof reference tracking are shown.

In Figure 32, $i_1$, $i_2$, $i_3$ and $i_4$ parameters occurring during 3-dof reference tracking are shown.

In Figure 33, the global-axis currents for 3-dof reference tracking are shown. Because of 3-dof motion, $i_z$, $i_\alpha$ and $i_\beta$ are non-zero values.

## 5.2. Disturbance rejection case

The disturbance rejection case is conducted for only I-PD controlled system. This case investigates the reference tracking performance of the system under a mechanical disturbance. And the desired references, $\alpha_{ref}$, $\beta_{ref}$ and $z_{ref}$ are zero. The load shown in Figure 34
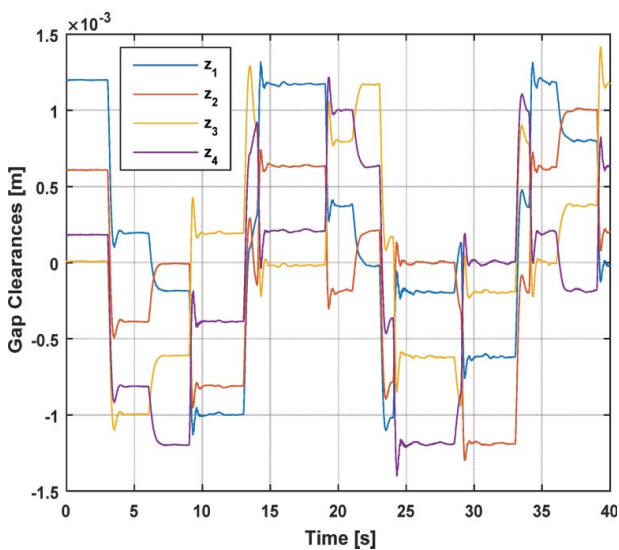


**Figure 31.** $z_1$, $z_2$, $z_3$ and $z_4$ parameters occurring during 3-dof reference tracking for CDM-based I-PD controller.
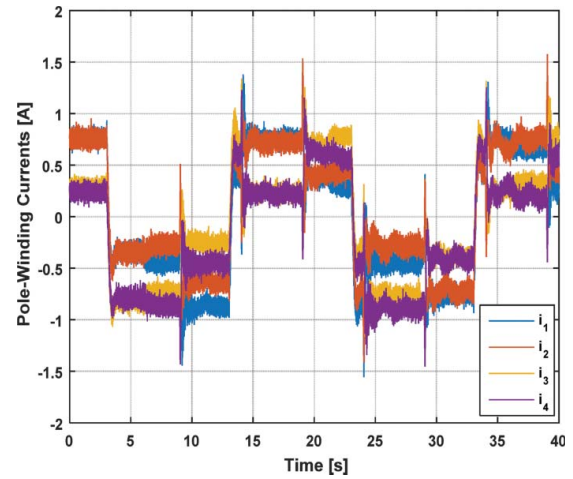


**Figure 32.** $i_1$, $i_2$, $i_3$ and $i_4$ parameters occurring during 3-dof reference tracking for CDM-based I-PD controller.
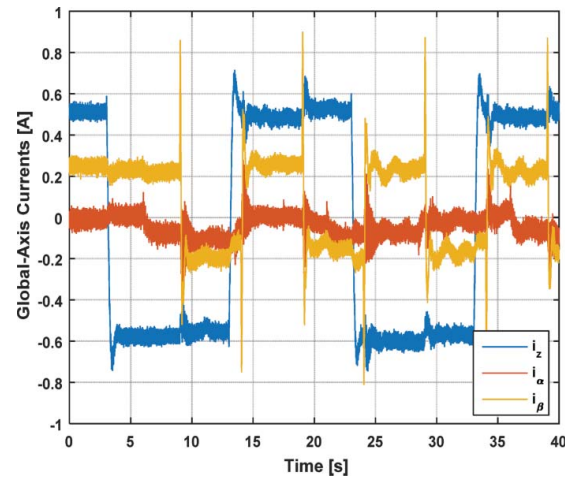


**Figure 33.** $i_z$, $i_\alpha$ and $i_\beta$ parameters occurring during 3-dof reference tracking for CDM-based I-PD controller.
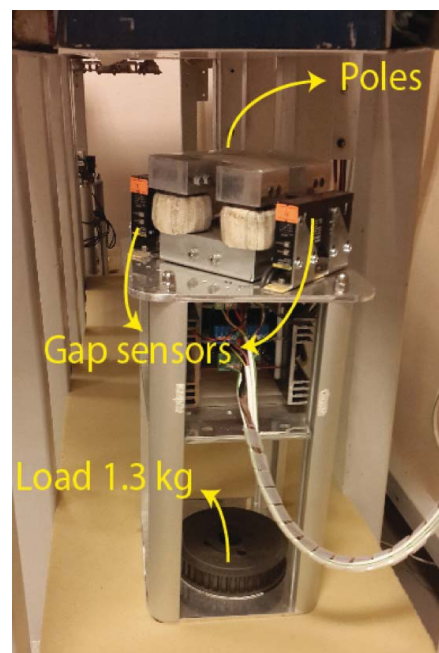
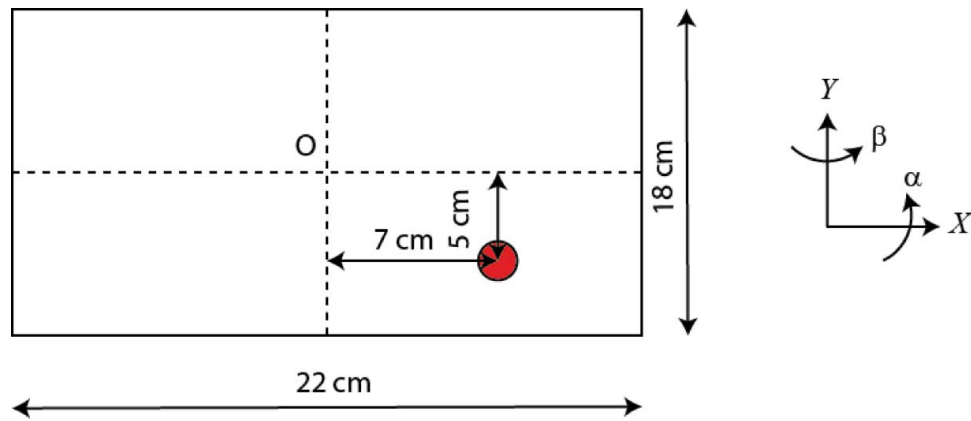

**Figure 34.** The load as an external disturbance.

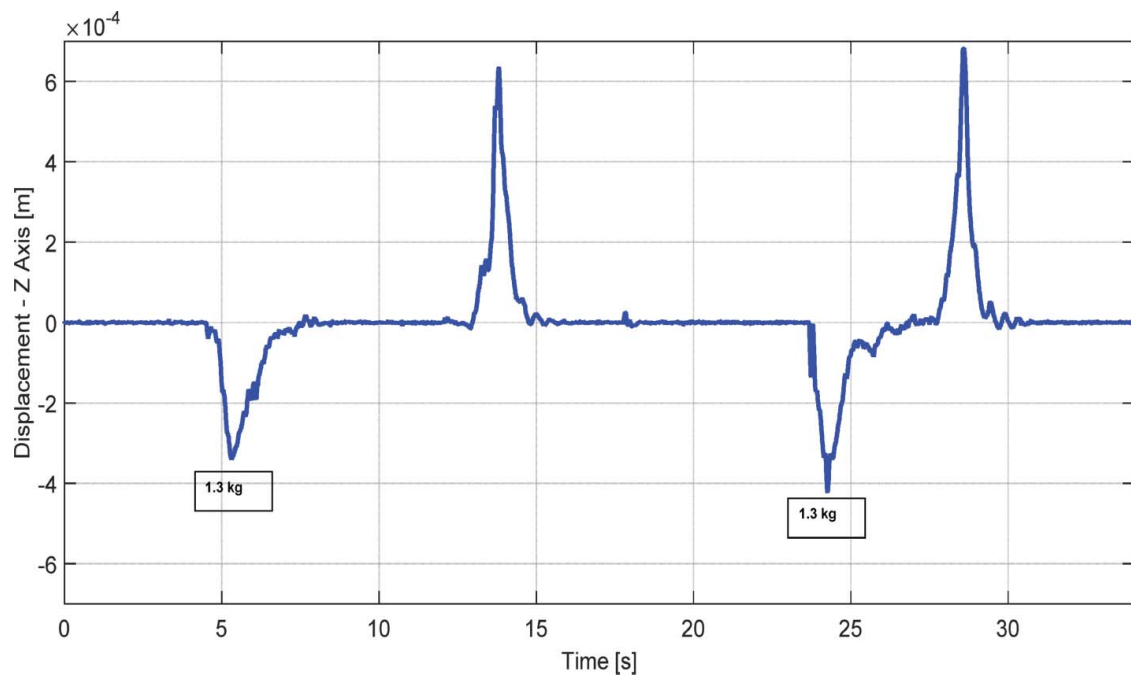**Figure 35.** The exact position of the applied load.



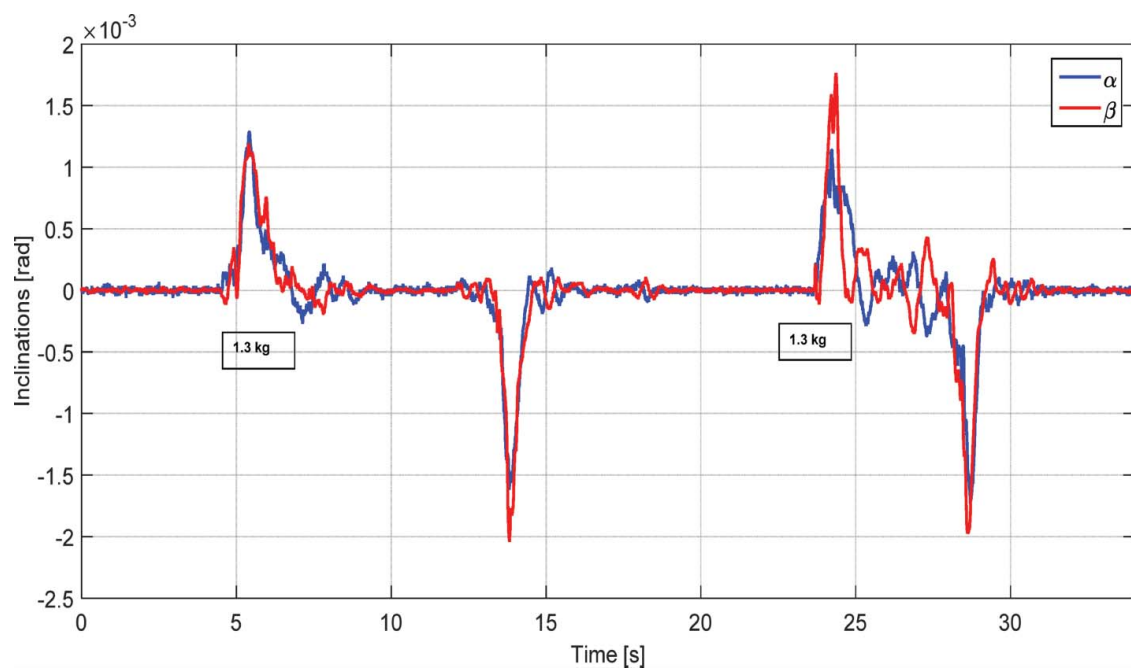**Figure 36.** External disturbance compensation performance of CDM-based I-PD controller for *Z*-axis.



**Figure 37.** External disturbance compensation performance of CDM-based I-PD controller for *X*($\alpha$) and *Y*($\beta$) axis.
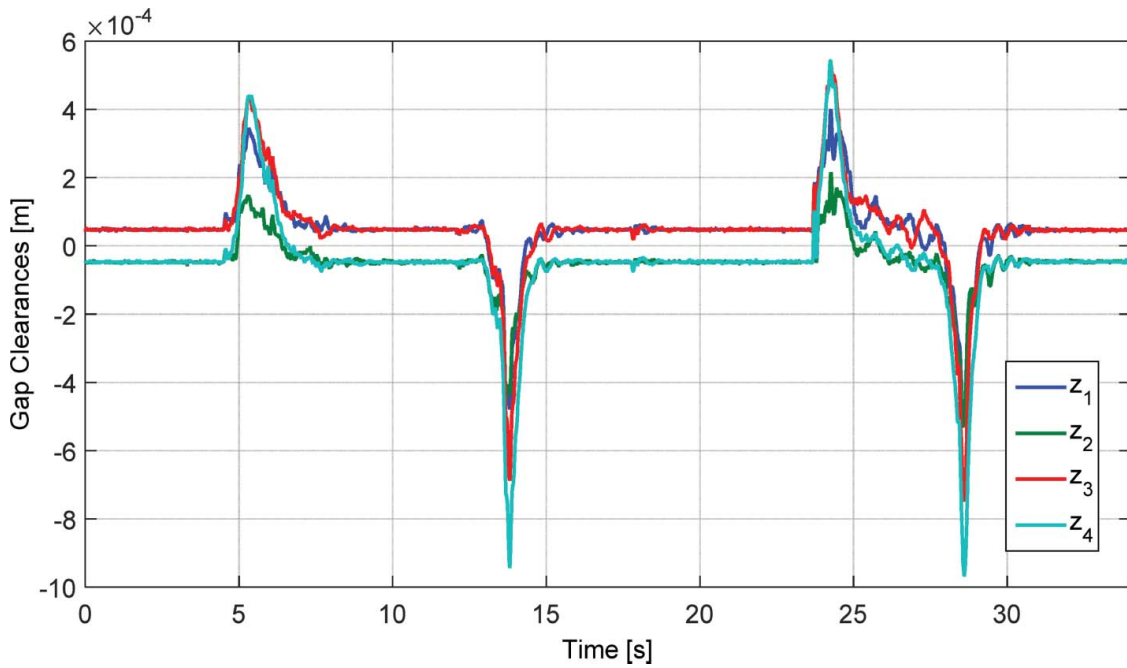
**Figure 38.** $z_1$, $z_2$, $z_3$ and $z_4$ parameters occurring during the external disturbance.

is applied as an external disturbance on the system. The exact position of the applied load can be seen in Figure 35.

So that, the moment value occurred around the $X$-axis is 0.63 Nm and the moment value occurred around the $Y$-axis is 0.88 Nm.

In Figure 36, it can be seen that when the load is applied at the fifth second, a deflection starts occurring for 2 s, and then the system is getting stabilized. When the applied load is removed from the system at the 13th second, another deflection starts occurring for 2 s

to the opposite direction, and then the system is getting stabilized again. The same situations occur at 23rd and 27th seconds as well.

In Figure 37, the inclinations of $\alpha$- and $\beta$-axes when the load is applied are shown. The stabilization time is 2 s for both $\alpha$- and $\beta$-axes.

In Figure 38, $z_1$, $z_2$, $z_3$ and $z_4$ parameters occurring during the external disturbance can be seen. The reason of the difference between $z_1$, $z_2$, $z_3$ and $z_4$ parameters is the moment occurring due to the position of the load.
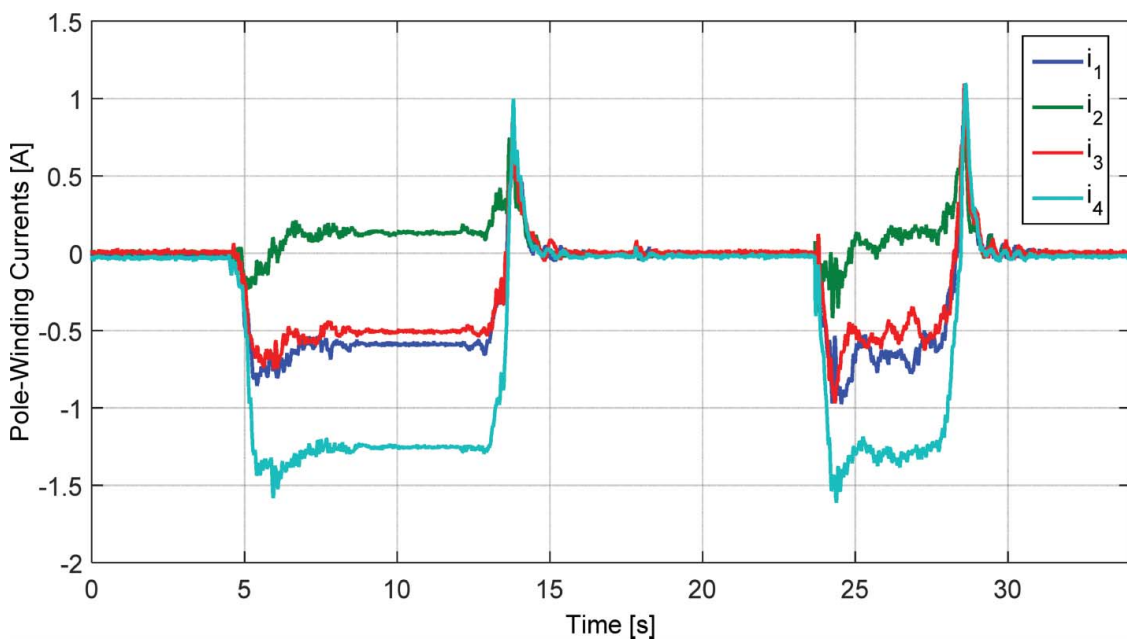


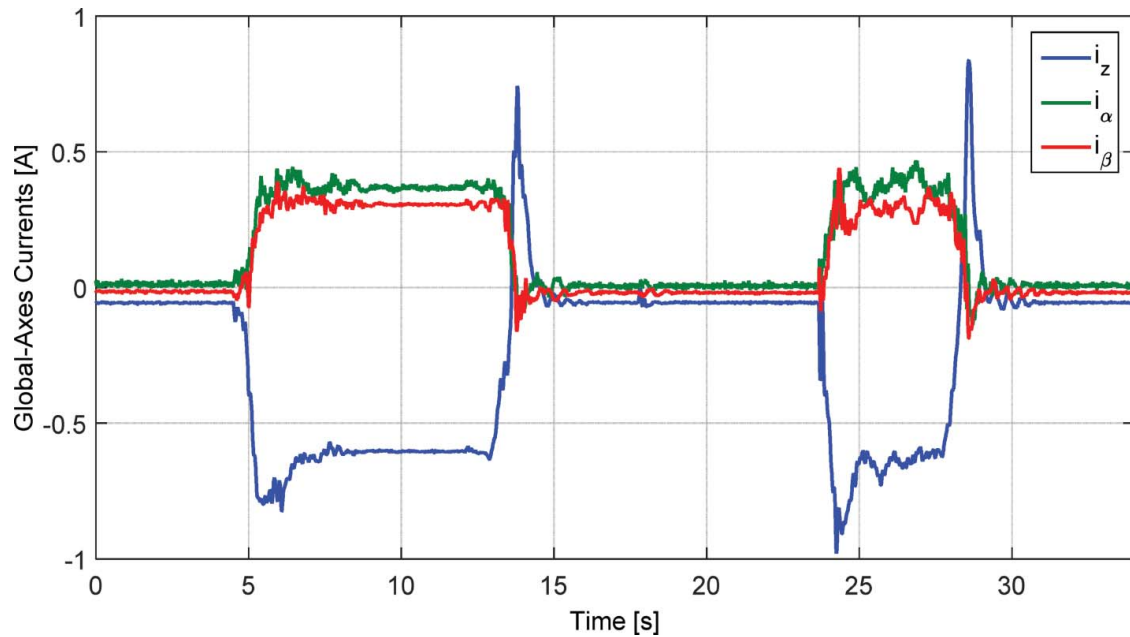**Figure 39.** $i_1$, $i_2$, $i_3$ and $i_4$ parameters occurring during the external disturbance.

**Figure 40.** $i_z$, $i_\alpha$ and $i_\beta$ parameters occurring during the external disturbance.

In Figure 39, $i_1$, $i_2$, $i_3$ and $i_4$ parameters occurring during the external disturbance are shown. The reason of the difference between $i_1$, $i_2$, $i_3$ and $i_4$ parameters is the moment occurring due to the position of the load.

In Figure 40, the global-axis currents are shown. As can been seen, $i_\alpha$ and $i_\beta$ values follow the same pattern, the main reason of this situations is that the moment value around the $X(\alpha)$ axis, 0.63 Nm, and the moment value around the $Y(\beta)$ axis, 0.88 Nm, are close to each other.

## 6. Conclusion

In this study, it has been proven that the outlined CDM for synthesizing I-PD and PID controller coefficients is a suitable and relatively easy, and applicable for controlling 3-dof motion of 4-pole hybrid electromagnetic systems.

Reference tracking performances of both I-PD and PID controllers for each axis have been tested and evaluated using step reference inputs. I-PD controller performs almost a perfect reference tracking ability for each axis of 4-pole hybrid electromagnet.

Reference tracking performance of I-PD controller for each axis has also been tested and evaluated for a disturbance rejection case. It has been proven that robust reference tracking control can be achieved with the proposed I-PD controller.

A review has been conducted between the proposed control method and other control methods popularly used for magnetic levitation applications, such as sliding mode control, fuzzy logic control. It has clearly been stated that the proposed method is more appropriate for industrial applications in terms of computational simplicity, visualization of controller dynamics and easy-tuning.

The proposed technique has an appropriate potential to apply any kind of magnetic motion control system without sacrificing a good balance point among simplicity, robustness, stability and speed of response via visual design support. The experimental results validate effectiveness of the proposed controller design method for motion control of 4-pole hybrid electromagnet.

## Disclosure statement

The authors declare that there is no conflict of interests regarding the publication of this paper.

## Funding

## References

1. Erkan K, Koseki T. Fuzzy model-based nonlinear maglev control for active vibration control systems. Int J Appl Electromagn Mech. 2007;25:543–548.
2. Yakushi K, Koseki T, Sone S. 3 degree-of-freedom zero power magnetic levitation control by a 4-pole type electromagnet. International Power Electronics Conference; 2000; Tokyo, Japan.
3. Liu J, Yakushi K, Koseki T, et al. 3 degrees of freedom control of zero-power magnetic levitation for flexible transport system. The 16th International Conference on Magnetically Levitated Systems and Linear Drives; 2000; Rio de Janeiro, Brazil.
4. Jiangheng L, Koseki T. 3 degrees of freedom control of semi-zero-power magnetic levitation suitable for two-

dimensional linear motor. Proceedings of the Fifth International Conference on Electrical Machines and Systems, 2001. ICEMS 2001; 2001 Aug 18–20; Shenyang, China.

5. Furlani EP. Permanent magnet and electromechanical devices. San Diego (CA): Academic Press; 2001.

6. Sung-Kyung H, Langari R. Robust fuzzy control of a magnetic bearing system subject to harmonic disturbances. IEEE Trans Contr Syst Technol. 2000;8 (2):366–371.

7. Hoque ME, Mizuno T, Ishino Y, et al. A six-axis hybrid vibration isolation system using active zero-power control supported by passive weight support mechanism. J Sound Vib. 2010;329(17):3417–3430.

8. Hoque ME, Mizuno T, Ishino Y, et al. A three-axis vibration isolation system using modified zero-power controller with parallel mechanism technique. Mechatronics. 2011;21(6):1055–1062.

9. Mizuno T, Takasaki M, Kishita D, et al. Vibration isolation system combining zero-power magnetic suspension with springs. Control Eng Pract. 2007;15 (2):187–196.

10. Baig JI, Mahmood A. Robust control design of a magnetic levitation system. 19th International Multi-Topic Conference (INMIC); 2016 Dec 5–6; Islamabad, Pakistan.

11. Rezgui M, Ayadi HB, Braiek NB. Local stabilizing control with maximization of stability domain for a magnetic levitation system via polynomial modeling. 16th International Conference on Sciences and Techniques of Automatic Control and Computer Engineering (STA); 2015 Dec 21–23; Monastir, Tunisia.

12. Raja CVN, Ananthababu P, Pushpa Latha DV, et al. Design and analysis of position controlled eddy current based nonlinear magnetic levitation system using LMI. International Conference on Control Communication & Computing India (ICCC); 2015 Nov 19–21; Trivandrum, India.

13. Venghi LE, Gonzalez GN, Serra FM. Implementation and control of a magnetic levitation system. IEEE Lat Am Trans. 2016;14(6):2651–2656.

14. Unni AC, Junghare AS, Mohan V, et al. PID, fuzzy and LQR controllers for magnetic levitation system. International Conference on Cogeneration, Small Power Plants and District Energy (ICUE); 2016 Sept 14–16; Bangkok, Thailand.

15. Bojan-Dragos CA, Preitl S, Precup R-E, et al. State feedback and proportional-integral-derivative control of a magnetic levitation system. IEEE 14th International Symposium on Intelligent Systems and Informatics (SISY); 2016 Aug 29–31; Subotica, Serbia.

16. Cho D, Kato Y, Spilman D. Sliding mode and classical controllers in magnetic levitation systems. IEEE Control Syst. 1993;13(1):42–48.

17. Chunfang L, Zhang J. Design of second-order sliding mode controller for electromagnetic levitation grip used in CNC. 24th Chinese Control and Decision Conference (CCDC); 2012 May 23–25; Taiyuan, China.

18. Chiang HK, Tseng W-T, Fang C-C, et al. Integral backstepping sliding mode control of a magnetic ball suspension system. IEEE 10th International Conference on Power Electronics and Drive Systems (PEDS); 2013 Apr 22–25; Kitakyushu, Japan.

19. Ertugrul HF, Erkan K. First order integral sliding mode control of the magnetically levitated 4-pole type hybrid electromagnet. International Conference on Engineering and Natural Sciences (ICENS); 2016 May 24–28; Sarajevo, Bosnia and Herzegovina.

20. Erkan K, Koseki T. Fuzzy model based nonlinear control of an active oscillation suppression system comprised of mechanically flexible elements and triple configuration of u-shaped electromagnets. 9th IEEE International Workshop on Advanced Motion Control; 2006 Mar 27–29; Istanbul, Turkey.

21. Su KH, Li CY. Supervisory fuzzy model control for magnetic levitation system. IEEE 13th International Conference on Networking, Sensing, and Control (ICNSC); 2016 Apr 28–30; México City, Mexico.

22. Kumar A, Kumar V. Performance analysis of Interval Type-2 FSM controller applied to a magnetic levitation system. International Conference on Soft Computing Techniques and Implementations (ICSCTI); 2015 Oct 8–10; Faridabad, India.

23. Nath A, Samantaray J, Chaudhury S. Magnetic ball levitation system control using sliding mode control and fuzzy PD+I control: a comparative study. International Conference on Energy, Power and Environment: Towards Sustainable Growth (ICEPE); 2015 June 12–13; Shillong, India.

24. Rodriguez H, Siguerdidjane H, Ortega R. Experimental comparison of linear and nonlinear controllers for a magnetic suspension. Proceedings of the 2000. IEEE International Conference on Control Applications. Conference Proceedings (Cat. No.00CH37162); 2000 Sept 27; Anchorage (AK).

25. Sarmad M, Ahmed S, Shami M, et al. Sampled data robust control for a magnetic levitation system—Some practical considerations. 13th International Bhurban Conference on Applied Sciences and Technology (IBCAST); 2016 Jan 12–16; Islamabad, Pakistan.

26. Zhang Y, Xian B, Ma S. Continuous robust tracking control for magnetic levitation system with unidirectional input constraint. IEEE Trans Ind Electron. 2015;62(9):5971–5980.

27. Ahsan M, Masood N, Wali F. Control of a magnetic levitation system using non-linear robust design tools. 3rd IEEE International Conference on Computer, Control and Communication (IC4); 2013 Sept 25–26; Karachi, Pakistan.

28. Singh B, Kumar V. A real time application of model reference adaptive PID controller for magnetic levitation system. IEEE Power, Communication and Information Technology Conference (PCITC); 2015 Oct 15–17; Bhubaneswar, India.

29. Atlihan M, Bucak M, Erkan K. Horizontal I-PD position control of a levitated hybrid electromagnet driven by 3 phase ac long stator L-PMSM. International Aegean Conference on Electrical Machines & Power Electronics (ACEMP), 2015 Intl Conference on Optimization of Electrical & Electronic Equipment (OPTIM) & 2015 Intl Symposium on Advanced Electromechanical Motion Systems (ELECTROMOTION); 2015 Sept 2–4; Side, Turkey.

30. Verma SK, Yadav S, Nagar SK. Optimal fractional order PID controller for magnetic levitation system. 39th National Systems Conference (NSC); 2015 Dec 14–16; Noida, India.

31. Coelho JP, Boaventura-Cunha J, de Moura Oliveira PB, Extended stability conditions for CDM controller design. In: PA Moreira, A Matos, and G Veiga, editors. CONTROLO'2014 – Proceedings of the 11th Portuguese Conference on Automatic Control; Cham: Springer International Publishing; 2015. p. 171–182.

32. Ucar A, Hamamci SE. A controller based on coefficient diagram method for the robotic manipulators. ICECS 2000. 7th IEEE International Conference on Electronics, Circuits and Systems (Cat. No.00EX445); 2000 Dec 17–20; Jounieh, Lebanon.

33. Hamamci SE, Koksal M. Robust controller design for TITO processes with coefficient diagram method. Proceedings of 2003 IEEE Conference on Control Applications, 2003. CCA 2003; 2003 June 25; Istanbul, Turkey.

34. Koksal M, Hamamci SE. Robust temperature control of MSF desalination plants with coefficient diagram method. Proceedings of 2003 IEEE Conference on Control Applications, 2003. CCA 2003; 2003 June 25; Istanbul, Turkey.

35. Hamamci SE, Ucar A. A robust model-based control for uncertain systems. Trans Inst Meas Control. 2002;24 (5):431–445.

36. Erkan K, Acarkan B, Koseki T. Zero-power levitation control design for a 4-pole electromagnet on the basis of a transfer function approach. IEEE International Electric Machines & Drives Conference; 2007 May 3–5; Antalya, Turkey.

37. Erkan K, Okur B, Koseki T, et al. Experimental evaluation of zero-power levitation control by transfer function approach for a 4-pole hybrid electromagnet. IEEE International Conference on Mechatronics; 2011 Apr 13–15; Istanbul, Turkey.

38. Lipatov AV, Sokolov N. Some sufficient conditions for stability and instability of continous linear stationary systems. Automat Remote Control. 1979;39: 1285–1291.

39. Manabe S. Coefficient diagram method. 14th IFAC Symposium on Automatic Control in Aerospace; 1998; Seoul, South Korea.